Wetting mechanisms at the microscale: From classical models to topological pinning

Chenyang Wu(吴晨阳), Dongdong Lin(林冬冬)

Citation: Chin. Phys. B. 35, 106801 (2026). DOI: 10.1088/1674-1056/ae9a5c | CSTR: 32038.14.CPB.ae9a5c
http://cpb.iphy.ac.cn; http://iopscience.iop.org/cpb

What follows is a list of articles you may be interested in

Three-dimensional flat bands and possible interlayer triplet pairing superconductivity in the alternating twisted $NbSe_2$ moiré bulk

Shuang Liu(刘爽), Peng Chen(陈鹏), Shihao Zhang(张世豪)
Chin. Phys. B. 35, 026801 (2026). DOI: 10.1088/1674-1056/ae23ac | CSTR: 32038.14.CPB.ae23ac

Unchanged top surface-state structures in three-dimensional topological insulator Sb_2Te_3 thin films in the presence of bottom-surface moiré potentials

Dezhi Song(宋德志), Fuyang Huang(黄扶旸), Jun Zhang(仉君), Ye-Ping Jiang(蒋烨平)
Chin. Phys. B. 34, 126801 (2025). DOI: 10.1088/1674-1056/ae0926 | CSTR: 32038.14.CPB.ae0926

Mode characteristics of nested eccentric waveguides constructed by two cylindrical nanowires coated with graphene

Ji Liu(刘吉), Lixia Yu(于丽霞), Wenrui Xue(薛文瑞)
Chin. Phys. B. 31, 036803 (2022). DOI: 10.1088/1674-1056/ac1e17

Three-dimensional vertical ZnO transistors with suspended top electrodes fabricated by focused ion beam technology

Chi Sun(孙驰), Linyuan Zhao(赵林媛), Tingting Hao(郝婷婷), Renrong Liang(梁仁荣), Haitao Ye(叶海涛), Junjie Li(李俊杰), Changzhi Gu(顾长志)
Chin. Phys. B. 31, 016801 (2022). DOI: 10.1088/1674-1056/ac34fe

Analysis of meniscus beneath metastable droplets and wetting transition on micro/nano textured surfaces

Yanjie Li(李艳杰), Xiangqin Li(李香琴), Tianqing Liu(刘天庆), Weiguo Song(宋伟国)
Chin. Phys. B. 27, 086801 (2018). DOI: 10.1088/1674-1056/27/8/086801

TOPICAL REVIEW — A 40th Anniversary Celebration: Physics Research and Innovation at Ningbo University

Wetting mechanisms at the microscale: From classical models to topological pinning

Chenyang Wu(吴晨阳)[1,2] and Dongdong Lin(林冬冬)[1,2,†]

[1] *Institute of Fundamental Physics and Quantum Technology, Ningbo University, Ningbo* 315211, *China*
[2] *School of Physical Science and Technology, Ningbo University, Ningbo* 315211, *China*

(Received 30 May 2026; revised manuscript received 7 August 2026; accepted manuscript online 17 August 2026)

Wetting phenomena at the microscale govern critical interfacial behaviors, spanning natural self-cleaning surfaces and engineered microfluidic devices. Classical thermodynamics, formulated in the Young, Wenzel, and Cassie–Baxter models, forms the basis of static wettability. This review examines the transition from global interfacial tension minimization to topological wetting. In this approach, localized energy barriers at the three-phase contact line (TCL) largely determine macroscopic behavior. We analyze the microscopic origins of contact angle hysteresis (CAH) and pinning, showing that surface topology can outweigh intrinsic chemistry in defining apparent macroscopic wetting states. We highlight how closed-loop micro/nano structures impose continuous pinning, enabling programmable control of droplet adhesion and anisotropic transport independent of material chemistry. Furthermore, we discuss practical applications of these principles in anti-icing, microdroplet reactors, and self-cleaning surfaces, emphasizing the role of structural optimization in overcoming the durability–functionality trade-off. Finally, we outline future challenges in the field. We propose that integrating artificial intelligence (AI)-driven inverse design and adaptive "4D" interfaces will advance wetting science from a descriptive discipline into a precise engineering toolkit based on dynamic contact line energy.

Keywords: topological wetting, contact line pinning, three-phase contact line (TCL), contact angle hysteresis (CAH), micro/nano structures

PACS: 68.08.Bc, 47.55.D–, 68.03.–g

DOI: 10.1088/1674-1056/ae9a5c **CSTR:** 32038.14.CPB.ae9a5c

1. Introduction

Wetting phenomena govern critical interfacial behaviors in both natural systems and engineering applications, ranging from the directional transport of dewdrops on biological surfaces to the precise manipulation of microdroplets in microfluidic chips.[1–4] At its fundamental level, wetting represents a dynamic equilibrium of molecular forces at the vapor–liquid–solid three-phase interface. As classically unified by de Gennes, the comprehensive picture of wetting inherently couples the statics of physical chemistry with the complex fluid dynamics of the spreading contact line.[5] Historically, the theoretical framework of wetting was established by Thomas Young in 1805, who defined the static contact angle θ_Y as the result of a force balance among interfacial tensions.[6] While Young's equation provides the thermodynamic cornerstone, it describes an idealized state on rigid, chemically homogeneous, and smooth surfaces. In practice, however, real-world surfaces are usually inherently rough and chemically heterogeneous, leading to the phenomenon of contact angle hysteresis (CAH) — the discrepancy between the advancing and receding contact angles. Although subsequent models by Wenzel and Cassie–Baxter attempted to reconcile these deviations by introducing roughness factors and area fractions, they remain global averaging methods that often do not fully account for local pinning events. For instance, the coexistence of metastable states on re-entrant microstructures or the directional condensation on hydrophilic–hydrophobic patterns reveals that wetting is not merely a state function of surface energy, but a path-dependent process governed by energy barriers.[7]

Consequently, the field is currently undergoing a paradigm shift towards 'topology-dominated' wetting. In the context of this review, 'topological wetting' is precisely defined not merely as wetting influenced by general surface roughness or arbitrary geometrical constraints, but as macroscopic wetting behavior strictly governed by the global connectivity and spatial continuity of surface structural features. The classical view, which focuses on modifying intrinsic surface energy (e.g., surfactant adsorption or chemical coating), is being superseded by the concept of topological wetting. Recent investigations utilizing high-speed atomic force microscopy (AFM) and molecular dynamics (MD) simulations have demonstrated that the three-phase contact line (TCL) is not a continuous boundary but a discrete entity subject to "stick–slip" dynamics.[8–12] Crucially, closed-loop micro/nano structures (characterized by a topological genus

[†]Corresponding author. E-mail: lindongdong@nbu.edu.cn

© 2026 Chinese Physical Society and IOP Publishing Ltd. All rights, including for text and data mining, AI training, and similar technologies, are reserved.

$g = 1$) can impose continuous pinning independent of the material's intrinsic chemistry, enabling the rational design of surfaces with programmable adhesion and anisotropic transport properties. This topological approach addresses the limitations of traditional theories by treating the contact angle as a variable constrained by local geometric energy barriers rather than a fixed material constant. This interaction profoundly influences diverse technological processes: in the energy sector, the wettability of lithium-ion battery electrodes dictates ion transport efficiency, where plasma-treated graphene networks optimize electrolyte permeability;[13–15] similarly, in biomimetic engineering, superhydrophobic surfaces rely on hierarchical micro/nano structures to drastically reduce fluid drag, emulating the water-repellency of xylem ducts or lotus leaves.[16–18]

Despite these conceptual advances, the translation of topological principles into functional applications faces significant hurdles. The complexity of dynamic interfaces under external perturbations — such as thermal gradients or mechanical vibrations — requires non-equilibrium models that exceed the scope of classical thermodynamics.[19–24] Furthermore, the durability of superwetting surfaces remains a critical bottleneck; high-aspect-ratio topological structures are susceptible to degradation in harsh environments, necessitating novel strategies for mechanical reinforcement and self-healing.[25] A paradigm-shifting solution to this fragility is the development of bioinspired slippery liquid-infused porous surfaces (SLIPS), which abandon the trapped-air mechanism in favor of a locked-in lubricating fluid, thereby creating a defect-free, self-repairing interface capable of maintaining omniphobicity even under extreme pressure.[26] Addressing these challenges requires a synergistic approach integrating multiscale structural regulation, stimuli-responsive materials, and intelligent adaptive design.[27,28]

This review provides a comprehensive synthesis of the evolution of wetting science, moving from classical models to the emerging framework of topological pinning. We first revisit the thermodynamic foundations and critically analyze the limitations of the Young, Wenzel, and Cassie–Baxter models in describing complex interfaces. Subsequently, we elucidate the mechanism of wetting hysteresis and contact line pinning, highlighting how multi-scale substrate design — specifically topological constraints — can precisely regulate wetting behavior beyond the limits of surface chemistry. To bridge theory and practice, we evaluate advanced characterization techniques, including axisymmetric droplet shape analysis (ADSA-P) and *in situ* multiscale imaging, which are essential for resolving invisible contact line dynamics. Finally, we discuss the transformative applications of these principles in anti-icing, microdroplet reactors, and self-cleaning surfaces, concluding with an outlook on the future challenges of environmental stability and artificial intelligence (AI)-driven intelligent design.

2. Classical wetting models and their thermodynamic limits

Liquid–solid interactions govern critical interfacial phenomena. While the classical Young, Wenzel, and Cassie–Baxter models predict macroscopic wettability through global free energy minimization, their validity range is heavily restricted. Specifically, these frameworks frequently encounter limitations on textured surfaces or within multiphase environments.

2.1. Ideal equilibrium: Young's equation

The systematic theory of wetting quantifies the interplay between interfacial tensions and the equilibrium contact angle.[6,29] Consider a liquid droplet on an ideal, chemically homogeneous, and physically flat solid surface. By analyzing the principle of minimization of surface free energy, one can apply a virtual displacement δx to the TCL along the solid surface (Fig. 1). The variation in the total interfacial free energy per unit length is expressed as

$$\delta G = (\gamma_{SL} - \gamma_{SV})\delta x + \gamma_{LV}\cos\theta_Y \delta x,$$

where γ_{SV}, γ_{SL}, and γ_{LV} represent the interfacial tensions of solid–vapor, solid–liquid, and liquid–vapor. The first term represents the work done by replacing the solid–vapor interface with the solid–liquid interface, and the second term accounts for the projection of the liquid–vapor tension along the displacement vector.[6] At thermodynamic equilibrium, $\delta G = 0$ for any δx; this yields the famous Young's equation (often referred to as the Young–Gibbs relation[30])

$$\gamma_{SV} = \gamma_{SL} + \gamma_{LV}\cos\theta_Y. \tag{1}$$

The equation implies that for a given set of materials, there exists a unique, intrinsic contact angle θ_Y determined solely by the balance of interfacial tensions (γ_{SV}, γ_{SL}, γ_{LV}), as illustrated in Fig. 1.[6,31] However, the applicability of Young's equation is strictly confined to ideal conditions. It presumes a featureless substrate, thereby ignoring the roles of surface roughness, chemical heterogeneity, and body forces such as gravity and viscosity.[32–34] A fundamental contradiction arises when applying this model to real surfaces: Young's equation predicts a single global energy minimum, whereas experimental observations universally demonstrate CAH. On microstructured surfaces, this hysteresis often exceeds 40°,[35,36] far beyond the standard range (5°–20°) and the scope of Young's static prediction.[32,34]

This discrepancy highlights a critical theoretical limitation: Young's equation treats the contact line as a geometric

singularity without energy barriers. It decouples the static contact angle from the complex energy landscape created by surface topography.[31,33] As we will discuss, on real surfaces, the wetting state is often trapped in metastable states governed by local pinning forces, rather than the global area-averaged tensions assumed in the classic thermodynamic framework.[6,34] To address the fundamental limitations of Young's equation regarding surface topography, the early 20th-century advancements focused on thermodynamic modifications based on global area-averaging. Unlike Young's model, which assumes an ideal plane, these models posit that the apparent contact angle is determined by the statistical average of surface energies over the entire contact area.[37,38]

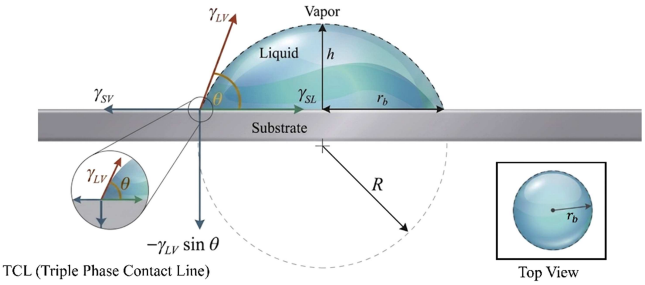

Fig. 1. Schematic of a sessile droplet on a flat substrate. Key parameters are defined: h (droplet height), R (droplet radius of curvature), r_b (contact radius). The equilibrium is governed by the interfacial tensions: γ_{SV} (solid–vapor), γ_{LV} (liquid–vapor), and γ_{SL} (solid–liquid).

2.2. Area-averaged approximations: Wenzel and Cassie–Baxter models

2.2.1. The Wenzel state: roughness-induced amplification

Starting from Young's relation, for a rough surface, Wenzel assumed that the liquid completely penetrates the asperities of the solid, thereby increasing the actual solid–liquid contact area. If the roughness factor r is defined as the ratio of the true solid–liquid interfacial area to its projected geometric area

$$r = A_{\text{real}}/A_{\text{proj}} > 1. \tag{2}$$

To derive the Wenzel equation, consider a virtual displacement of the apparent contact line by a distance δx. The change in free energy per unit width is

$$\delta G = r(\gamma_{SL} - \gamma_{SV})\,\delta x + \gamma_{LV}\cos\theta_W\,\delta x.$$

At equilibrium, $\delta G = 0$, so

$$r(\gamma_{SL} - \gamma_{SV}) + \gamma_{LV}\cos\theta_W = 0.$$

Rearranging and substituting Young's equation $\left(\cos\theta_Y = (\gamma_{SV} - \gamma_{SL})/\gamma_{LV}\right)$ yields

$$\cos\theta_W = r\cos\theta_Y. \tag{3}$$

This is known as the Wenzel equation. The model reveals the nonlinear regulation mechanism of roughness on the apparent contact angle as shown in Fig. 2(a). When the static contact angle $\theta_Y > 90°$, the surface topology significantly enhances the hydrophobicity by increasing the effective contact area. When $\theta_Y < 90°$, roughness improves hydrophilicity (approaching 0°) by enhancing the liquid–solid interaction. For example, when $\theta_Y = 120°$ and $r = 3$, theoretical calculations show that the apparent contact angle can be increased to 163°, and the exponential enhancement effect of hydrophobicity is verified experimentally, such as laser etching of micro/nano composite structures on the surface of aluminum.[32]

However, it is crucial to note that the Wenzel model assumes thermodynamic equilibrium where the liquid completely wets the grooves. It remains unclear whether this configuration corresponds to the global minimum free-energy state of the system, particularly for hydrophobic or chemically heterogeneous surfaces.[39] Furthermore, the model cannot account for CAH or the significant increase in the rolling angle often observed on superhydrophobic surfaces,[29] necessitating the consideration of heterogeneous wetting states.

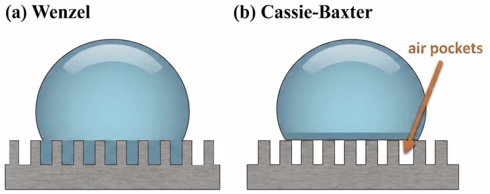

Fig. 2. (a) Wenzel state: The liquid completely infiltrates the surface grooves, resulting in a homogeneous solid–liquid interface without air entrapment. (b) Cassie–Baxter state: The liquid sits atop the surface asperities, forming a composite interface with trapped air pockets (indicated by orange arrows) within the microgrooves. Note that the Cassie state typically refers to chemical heterogeneity on flat surfaces, whereas the Cassie–Baxter state involves topological roughness with air inclusions.

2.2.2. The Cassie–Baxter state: composite interface and air trapping

The limitations of the Wenzel model stem from its neglect of air trapping effects and surface chemical heterogeneity.[40,41] To overcome these limitations, Cassie and Baxter proposed the "air pockets" model,[42,43] as shown in Fig. 2(b), which elucidated the non-uniform wetting behavior of porous rough surfaces from a thermodynamic perspective for the first time. The model assumes that the liquid does not completely infiltrate the micro/nano structure of the solid surface, but traps the air between the solid–liquid interface through the topological bumps formed by the surface roughness, forming a composite interface composed of the solid–liquid contact region (area fraction f_{SL}) and the liquid–vapor contact region (area fraction f_{LV}). From a thermodynamic viewpoint, the apparent interfacial free energy per unit projected area can be written as

$$G = f_{SL}(\gamma_{SL} - \gamma_{SV}) + f_{LV}\gamma_{LV} + \gamma_{SV}.$$

Minimizing this free energy with respect to apparent contact angle θ_{CB} yields the equilibrium condition

$$\cos\theta_{CB} = f_{SL}\cos\theta_Y - f_{LV}, \tag{4}$$

where θ_Y is the static contact angle on a smooth surface. This expression corresponds to the Cassie–Baxter equation, which describes the apparent contact angle of a droplet resting on a composite solid–air interface.[43,44] When considering the microscopic roughness factor r, the Cassie–Baxter relation can be rewritten as

$$\cos\theta_{CB} = rf\cos\theta_Y + f - 1. \tag{5}$$

The physical connotation of this equation is reflected in two aspects. First, the intervention of the air phase significantly reduces the actual solid–liquid contact area ($f_{SL} < 1$), resulting in a decrease in adhesion (i.e., θ_{CB} approaches 180°). For example, when $f \to 0$ and $r \approx 1$, the theoretical contact angle can be increased to approximately 180°. Second, the roughness factor r further strengthens the hydrophobicity by amplifying the geometric effect of the surface topology, and this dual mechanism successfully explains the anomalously high apparent contact angle on biological surfaces.[43] It should be noted that the Cassie–Baxter model represents a special case of Cassie's general wetting model, where one of the surface components is air ($\theta_{air} = 180°$). In contrast, the original Cassie model applies to heterogeneous but flat surfaces composed of multiple solid materials without trapped air. This conceptual distinction is crucial for accurately describing wetting states and has often been a source of confusion in the literature. By comparing the Wenzel and Cassie–Baxter relations ($\cos\theta_W$ and $\cos\theta_{CB}$), the critical static contact angle for the Cassie–Wenzel transition can be derived as

$$\cos\theta_c = \frac{f-1}{r-f}. \tag{6}$$

When the static contact angle $\theta_Y > \theta_c$, the air layer can remain stable, and the droplets show low adhesion and superhydrophobicity. On the contrary, the Cassie–Wenzel wetting transition occurs, and the CAH increases significantly. This theoretical framework not only bridges the Wenzel and Cassie–Baxter regimes but also provides design guidance for robust superhydrophobic surfaces.

It should be noted that the derivation of the critical contact angle θ_c here is based on a direct comparison of the apparent energies of the Cassie–Baxter and Wenzel states. This classical criterion assumes an idealized situation in which no energy barrier exists between the two states. However, real textured surfaces typically exhibit a finite energy barrier separating the Cassie state from the Wenzel state, implying that the Cassie state may remain metastable even when the Wenzel state has a lower free energy. Therefore, the value of θ_c obtained here should be interpreted as a thermodynamic limit rather than an actual transition point, which is additionally governed by the magnitude of the energy barrier. Furthermore, comprehensive thermodynamic analyses reveal that the existence of the heterogeneous Cassie regime requires strict geometrical conditions; if these are violated, the droplet spontaneously collapses into the homogeneous Wenzel state even when the Cassie–Baxter equation appears mathematically satisfied.[45] This design strategy has been widely used in self-cleaning,[29,32] anticing surfaces (e.g., power grid insulators), and oil–water separation membranes.[46]

While these area-averaged models provide a foundational framework, their reliance on global energy minimization often does not fully capture the complexity of real wetting systems, particularly CAH and pinning. As we will discuss in the next section, these dynamic behaviors are fundamentally governed by the specific interactions at the three-phase contact line, rather than the average surface area.

2.3. Wetting transitions and metastability

The transition between the Wenzel and Cassie–Baxter states represents a critical phenomenon that determines the stability and durability of superhydrophobic surfaces. In real systems, these two wetting regimes are not mutually exclusive but rather coexist as metastable states separated by an energy barrier governed by capillary forces, surface geometry, and the intrinsic wettability of the substrate. When external pressure, condensation, or mechanical impact overcomes this barrier, the liquid–air interface penetrates the surface microcavities, triggering a spontaneous Cassie-to-Wenzel transition. As elucidated by Lafuma and Quéré, this transition is typically irreversible and is accompanied by a drastic shift in macroscopic adhesive properties, transforming a slippery, anti-adhesive surface into a highly pinned state.[47]

From a fundamental thermodynamic perspective, the shift between partial and complete wetting regimes behaves as a surface phase transition; the inherently first-order nature of this transition is the fundamental physical origin of observed metastable states and macroscopic hysteresis.[48] From a theoretical standpoint, the transition can then be interpreted as a free-energy barrier crossing process between two local minima in the Gibbs free energy landscape. Combined continuum theory and atomistic simulations have been used to calculate the free energy and grand potential profiles associated with this transition.[49] Their results, as shown in Figs. 3(a1)–3(a3) and 3(b1)–3(b8), indicated that the Cassie–Baxter state is inherently metastable, and nanoscale surface defects or thermal fluctuations can induce local meniscus depinning, asymmetric interface formation, and liquid finger propagation, ultimately collapsing the trapped air pocket inside the surface roughness. Building on these insights, subsequent analytical models and *in situ* confocal microscopy observations have shown that the critical transition pressure is governed by the interplay between Laplace capillary pressure and micropillar

topography,[50,51] as visualized in Figs. 3(c1)–3(c5). As evaporation proceeds, the water–air meniscus gradually sags, the air cushion thickness decreases continuously, and the local Laplace pressure increases accordingly. Once the destabilizing forces exceed the capillary restoring forces, the meniscus touches the bottom substrate, the entrapped air pockets lose stability abruptly, and liquid rapidly penetrates into the surface textures to complete the Cassie-to-Wenzel transition.

To quantify the magnitude of this barrier, the free-energy landscape of the transition pathway has been resolved, showing that it can reach tens to hundreds of nanojoules for millimetric droplets.[52] Similarly, analytical calculations for canonical surface geometries have confirmed that the Cassie state can persist as a metastable configuration even when the Wenzel state is thermodynamically more favorable.[53] These findings collectively reinforce that the "critical angle" derived in previous sections serves only as an equilibrium threshold, whereas the actual wetting transition is dynamically governed by the height of this energy barrier.

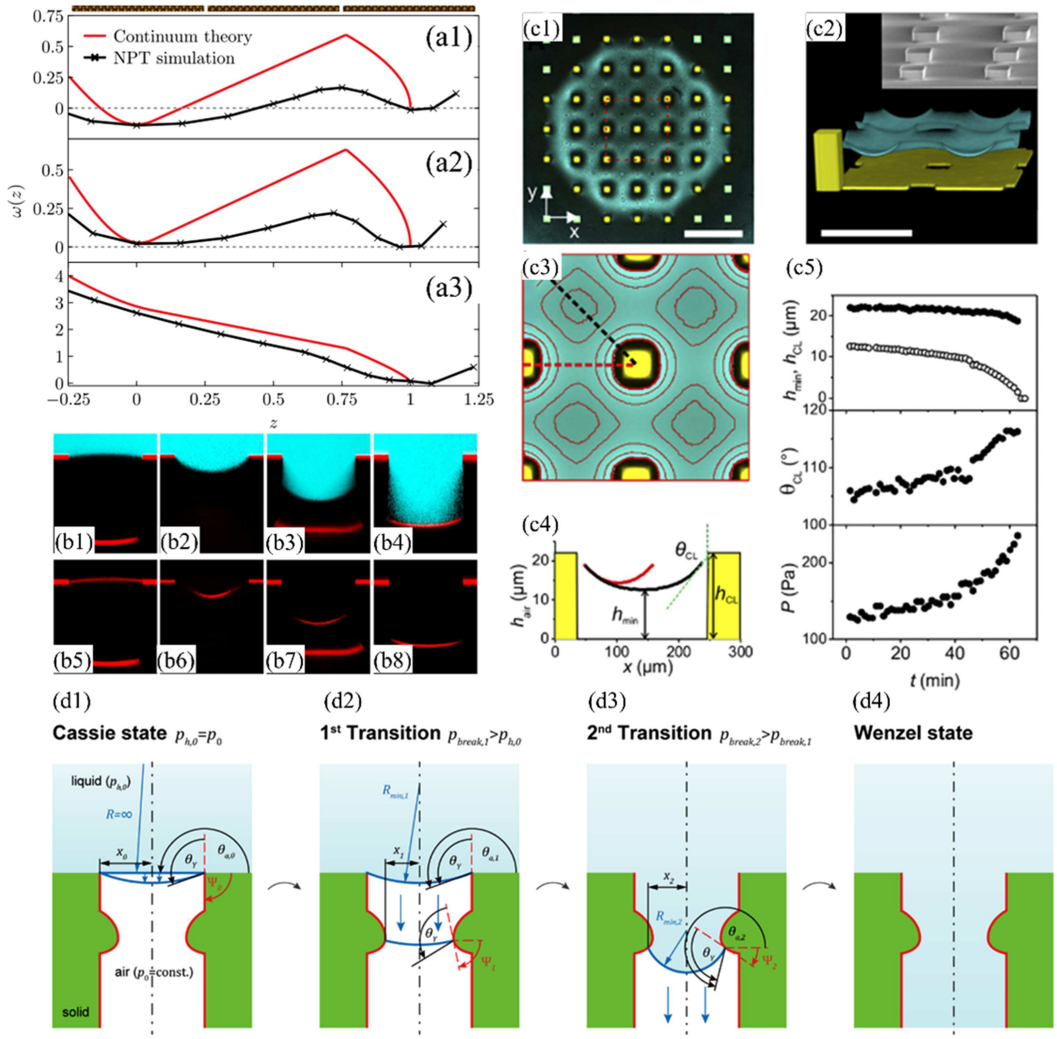

Fig. 3. Mechanism of the Cassie–Baxter to Wenzel transition from theoretical and experimental perspectives. (a1)–(a3) Free energy profiles from continuum theory (red) and NPT simulations (black) at $\Delta\tilde{p} = 0.01$, 0.17, 3.0. (b1)–(b8) Corresponding atomic configurations of liquid–vapor (b1)–(b4) and solid–liquid (b5)–(b8) interface evolution. (c1)–(c5) *In situ* confocal observation of air cushion sagging: (c1) top view, (c2) 3D reconstruction, (c3) thickness contour, (c4) meniscus schematic, (c5) evolution of height, contact angle and Laplace pressure. (d1)–(d4) Two-step wetting transition mechanism: (d1) Cassie state, (d2) contact line depinning, (d3) meniscus breakthrough, (d4) Wenzel state.[49,51,54] (Panels (a1)–(a3) and (b1)–(b8) reproduced with permission from Ref. [49] Copyright 2012, American Physical Society. Panels (c1)–(c5) reproduced with permission from Ref. [51] Copyright 2013, Proceedings of the National Academy of Sciences USA. Panels (d1)–(d4) reproduced from Ref. [54] under the ACS Author Choice License. Copyright 2014, American Chemical Society.)

Experimental evidence supports these theoretical insights, highlighting the role of surface topology in controlling contact line dynamics. *In situ* dark-field optical microscopy experiments on microstructured PFPEdma surfaces with well-defined cavity sidewall profiles have demonstrated that the sidewall geometry of surface microcavities governs both the breakthrough pressure and the wetting propagation pathway,[54] as illustrated in Figs. 3(d1)–3(d4). Straight vertical sidewalls allow early contact line depinning and uniform liquid infiltration, whereas re-entrant or overhanging sidewall features impose strong meniscus pinning, which elevates the transition pressure and significantly delays the col-

lapse of entrapped air pockets. Further *in situ* confocal studies on submerged micropore structures have confirmed that metastable intermediate states commonly appear between the ideal Cassie–Baxter and Wenzel regimes during the wetting transition,[55] with gradual meniscus sagging, contact line depinning, and dynamic partial infiltration driven by hydrostatic pressure and air diffusion, rather than an abrupt switch between the two states. Likewise, reversible Wenzel–Cassie restoration has also been observed under pressure release and bubble nucleation, emphasizing that the transition is not necessarily irreversible when trapped air re-emerges beneath the droplet.[56]

Recent investigations using molecular dynamics (MD) and lattice Boltzmann (LBM) simulations have further revealed the microscopic mechanisms underlying the transition. It has been summarized that the apparent contact angle hysteresis (CAH) in superhydrophobic systems originates from the coexistence of multiple metastable states and local meniscus pinning.[57] These studies collectively highlight that the CB–W transition is a dynamic and stochastic process rather than a single deterministic event.[49,54]

In summary, the Wenzel–Cassie transition represents the key to understanding the stability of superhydrophobicity. Crucially, the ability of a surface to maintain the metastable Cassie state depends on its capacity to "pin" the three-phase contact line against external disturbances. This realization shifts the focus from global area-averaged thermodynamics to the local mechanics of the contact line. As we will discuss in the next section, understanding these pinning forces requires a unified framework incorporating scale effects and line tension.

2.4. Limitations of global models: the role of contact line pinning

While the area-averaged Wenzel and Cassie–Baxter models have provided a foundational framework for macroscopic wetting, a growing body of experimental evidence indicates their limitations at the micro- and nanoscale. This limitation stems from the fact that these models treat wetting as a state function of the total interfacial area, whereas real wetting behavior is often governed by the specific interactions at the TCL.

Early studies first argued that the work of adhesion cannot be calculated simply by averaging the contact area, as local chemical differences along the contact line dictate the equilibrium state.[58] Pioneering theoretical models further established that while weak chemical heterogeneities merely distort the contact line, defects exceeding a critical strength trap the line in multiple stable positions, fundamentally generating the macroscopic advancing and receding angles.[59] This classical theory has since been elegantly validated on superhydrophobic models, demonstrating that even when the droplet rests on a perfectly slippery air cushion (the fakir state), the sharp edges of dilute micro-defects act as strong pinning sites that strictly dictate the macroscopic contact angle hysteresis as a function of defect density.[60] Subsequent experiments further confirmed this, showing that glycerol contact angles on rough paraffin surfaces (148°) differed significantly from smooth ones (98°), yet were governed by the contact line position rather than the wetted area.[41,61] More recent studies provided conclusive evidence.[62,63] As shown in Fig. 4, surfaces with concentric hydrophilic/hydrophobic zones were designed. It was found that when the droplet contact line was pinned at the outer edge of a hydrophobic ring, the contact angle was determined solely by the properties of that outer ring, independent of the hydrophilic area beneath the droplet. This result directly challenges the core assumption of the Cassie equation — that the contact angle is an area-weighted average — and confirms that the local interaction at the TCL is the dominant order parameter.

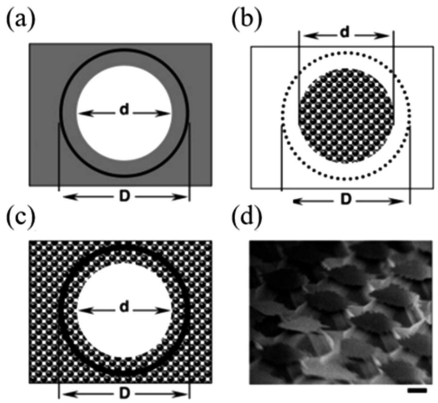

Fig. 4. Experiments designed by Gao–McCarthy. (a) The combined structure of the annular hydrophilic zone (diameter d) and the hydrophobic substrate (area width $D-d$); (b) annular rough areas on smooth substrates; (c) annular smooth area on rough substrate; (d) SEM image of the micropillar array in (b) and (c) (pillar diameter ≈ 5 μm, aspect ratio ≈ 3). The core conclusion is that when the droplet contact line is located at the outer edge of the annular region (region (2)), the wetting behavior is dominated by the substrate properties of the outer ring and is independent of the inner region.[32,41] (Reproduced with permission from Ref. [32] Copyright 2014, Elsevier.)

Statistical analysis further reinforces this conclusion. Statistical analysis of 166 micropatterned samples showed that the Cassie equation had a prediction error rate of 65% in cylindrical arrays and 44% in square cylindrical arrays.[64] Similarly, studies on closed-loop microstructures revealed contact angles exceeding 130° on surfaces where classical theory predicted 90°, proving that the TCL is pinned to the outer edge of the microwall structure.[65] Molecular dynamics simulations also show that for nanodroplets ($R < 10$ nm), the critical contact angle can fluctuate between 0° and 102.9°, deviating significantly from Young's prediction due to edge atomic interactions.[65] Indeed, early theoretical evaluations recognized these discrepancies, proposing that macroscopic wetting states and hysteresis are more accurately modeled by a linear average of the contact angle along the three-phase perimeter

— governed by contact line density — rather than the traditional area-averaged cosine.[66]

It is also crucial to note that classical models generally do not account for external body forces. When the droplet size approaches the millimeter scale or the liquid density is high, gravitational effects become comparable to capillary forces. This coupling induces asymmetric pressure fields and meniscus deformation, reducing the stability of the Cassie state and promoting gravity-assisted transitions.[67,68] Recent analyses reveal that gravity alters the critical transition threshold on microstructured substrates,[69,70] suggesting that the applicability of classical models should be carefully considered under realistic conditions where gravitational and interfacial effects coexist. Conversely, when the droplet size is comparable to the characteristic dimensions of the surface roughness, the breakdown of scale separation renders Wenzel and Cassie models less applicable.[71,72] In this intermediate regime, wetting is primarily influenced by discrete contact-line pinning rather than macroscopic area fractions.[73]

The physical origin of the "contact line dominance" lies in the molecular force imbalance at the TCL. As a one-dimensional boundary where vapor, liquid, and solid phases intersect, molecules at the contact line experience a highly asymmetric force environment, resulting in an additional energy contribution known as line tension.[74,75] The physical nature of this energy can be understood as a loss of conformational entropy of molecules in a confined space.[76]

The effect of line tension is scale-dependent and is quantified by the modified Young's equation[30,77,78]

$$\cos\theta = \cos\theta_{\mathrm{Y}} - \frac{\tau}{\gamma_{\mathrm{LV}} R}, \tag{7}$$

where R is the local radius of curvature of the contact line. Line tension typically ranges from 10^{-11} N to 10^{-6} N. As comprehensively reviewed, this wide variability in magnitude and sign reflects not only the diversity of solid–liquid–vapor systems but also the extreme sensitivity of experimental measurements to non-equilibrium conditions and theoretical oversimplifications.[79] For macroscopic droplets ($R \to \infty$), the term $\frac{\tau}{\gamma_{\mathrm{LV}} R}$ vanishes. However, for micro- or nanodroplets, or when the contact line is highly curved due to surface texture, this term becomes significant.[80,81] For example, on nanogrooved surfaces, a positive line tension forms a significant energy barrier, hindering contact line movement and becoming a central mechanism of CAH.[7,82]

Recognizing the limitations of area-based models, the theoretical basis of wetting is undergoing a theoretical transition to Gibbsian line thermodynamics. In this framework, the Gibbs adsorption equation[78] relates variations in interfacial tension to chemical potential changes along the contact line:

$$\mathrm{d}\gamma = -\sum \Gamma_i \mathrm{d}\mu_i. \tag{8}$$

Building on this, the Shardt–Elliott model reformulates the equilibrium contact angle in terms of the line fraction (f_{line}) of different components rather than the areal fraction, yielding a modified relation[83,84]

$$\cos\theta_{\mathrm{A}} = f_{1,\mathrm{line}}\cos\theta_{\mathrm{A},1} + f_{2,\mathrm{line}}\cos\theta_{\mathrm{A},2}. \tag{9}$$

This model has been shown to reduce prediction errors significantly. For instance, on striped surfaces where the Cassie equation error exceeded 15°, the Shardt–Elliott model prediction (65°) matched experimental data perfectly.[85] This confirms that the contact line fraction, rather than the area fraction, is the true governing parameter.

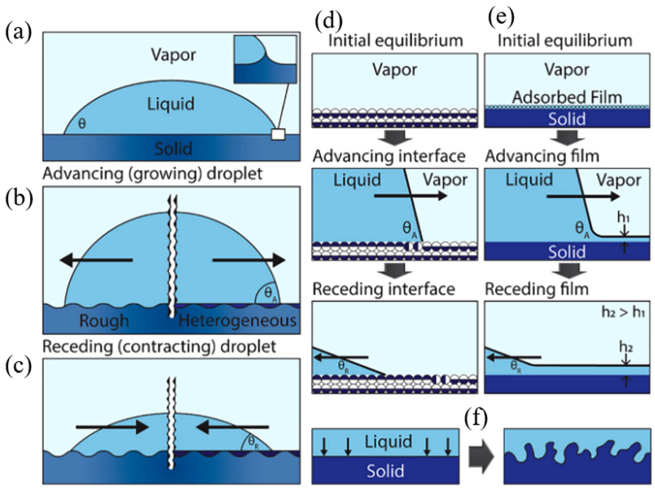

Fig. 5. Schematic diagram of droplets on a solid with different surface properties and CAH. (a) Droplets at rest on a flat solid surface: elastic and/or plastic deformation under the TCL caused by normal liquid stress and balanced by local stresses on the solid. (b) and (c) CAH caused by solid surface roughness (left) and inhomogeneity (right). (d) The difference in affinity of solid chemistry for non-polar gases and polar liquid phases is a cause of CAH. (e) The thin liquid film formed during the retreat of the liquid may be thicker than the precursor film formed during the spreading process. CAH is caused by different separation pressures. (f) Roughening of a smooth and uniform surface by swelling. Symbols include: H — liquid film thickness, θ — contact angle, θ_{A} — advancing contact angle, θ_{R} — receding contact angle.[88] (Reproduced with permission from Ref. [88] Copyright 2019, Elsevier.)

Finally, the magnitude of the line energy is precisely regulated by the geometric topology of the substrate. Abrupt changes in surface curvature, such as sharp edges or nanogrooves, create localized energy barriers that "pin" the contact line. This can be quantitatively described by the Huang equation[76]

$$\cos\phi = \frac{\gamma_{\mathrm{LV}}}{\gamma_{\mathrm{SV}}\kappa_{\mathrm{m}}} - \frac{\gamma_{\mathrm{SL}}}{\gamma_{\mathrm{LV}}}\cos\theta_{\mathrm{Y}}, \tag{10}$$

where κ is the local mean curvature. As shown in Fig. 5, high-density micropillar arrays induce a high degree of tortuosity in the contact line. Experiments show that reducing pillar spacing from 15 μm to 5 μm can triple the pinning energy barrier, raising CAH from 10° to 35°.[46] *In situ* AFM observations confirm that the pinning force at the edge of a nanogroove can require significant additional energy to overcome.[86,87]

The transition from area-averaged models to line-tension theories marks a critical maturation in wetting science. It reveals that the "super" properties of structured surfaces are not merely due to increased area, but are the result of engineering specific topological features — such as sharp edges and closed loops — that maximize contact line pinning. This understanding lays the physical foundation for the topological wetting strategies we will explore in the next section.

3. Engineering contact line pinning via surface topology

3.1. Stochastic roughness: random pinning networks

The most fundamental strategy to manipulate wetting is the introduction of stochastic surface roughness. Unlike ordered patterns, stochastic roughness — fabricated via methods such as chemical etching, deposition, or spraying — creates a disordered network of topological defects. These random asperities act as dense pinning sites that modify the global wetting behavior by altering the effective energy barriers at the TCL.

On intrinsically hydrophilic substrates, stochastic roughness creates a dense capillary network that amplifies wetting forces, driving the system deeply into the Wenzel regime. Experimental evidence demonstrates this through the deposition of nanoparticle films. For instance, a film with a roughness factor of $r \approx 2.49$–2.77 can induce a superhydrophilic state with contact angles as low as 15°–24°.[20,89] The underlying mechanism involves a synergy of geometric and chemical effects: First, the nanoscale pores (< 10 nm) within the stochastic network generate massive capillary pressures exceeding 10 MPa, which overcome local pinning barriers and drive the precursor liquid film to spread rapidly.[90] Second, surface defects play a critical role. For example, unsaturated bonds at the nanoparticle edges (e.g., Cd^{2+} dangling bonds) create a surface energy gradient that enhances the directional adsorption of water molecules. Studies indicate this can reduce the solid–liquid interfacial energy by approximately 38%.[91] Furthermore, under UV irradiation, photogenerated holes can oxidize surface hydroxyl groups, further reducing the contact angle to $\sim 9°$ and enhancing functional performance, such as achieving a 95% degradation rate for methyl orange.[92]

Conversely, on hydrophobic substrates, the random pinning network stabilizes the metastable Cassie–Baxter state by creating a high-density energy barrier against liquid intrusion. A prime example is the fluorinated graphene oxide (FGO)/polydimethylsiloxane (PDMS) nanocomposite coating. Here, the micron-scale average roughness ($R_a \approx 1.2$ μm) acts as primary anchor points for the contact line, providing a pinning energy barrier exceeding $100 k_B T$.[93] Simultaneously, the nanostructure of FGO sheets compresses the local radius of curvature of the liquid meniscus to ~ 10 nm. This extreme curvature invokes significant line tension effects, which fundamentally suppress the collapse of the air cushion by enhancing the depinning energy barrier.[94] This multi-scale stochastic pinning enables the surface to achieve a water contact angle of 173.7°, approaching the theoretical limit of 175°.[93] Molecular dynamics simulations further reveal that the stability of this state is sensitive to molecular orientation; for instance, a perfluoroalkyl chain inclination angle of $\sim 12°$ creates an optimal thermodynamic barrier of 25 kJ/mol, effectively preventing the transition to the Wenzel state.[90,93]

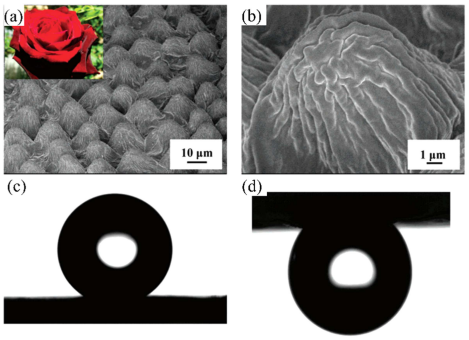

Fig. 6. The petal effect on stochastic hierarchical rough surfaces. (a), (b) SEM images of a red rose petal surface showing periodic micropapillae with nanofolds on each top. (c) A spherical water droplet on the petal surface with a contact angle of 152.4°, demonstrating superhydrophobicity. (d) A water droplet adheres firmly to the petal surface even when inverted, showing the high adhesive force characteristic of the petal effect.[95] (Reproduced from Ref. [95] under the ACS AuthorChoice License. Copyright 2008, American Chemical Society).

While stochastic roughness can stabilize the Cassie state, the lack of deterministic control over the contact line often leads to an intermediate regime known as the "petal effect".[95] Unlike the low-adhesion "lotus effect," surfaces like rose petals exhibit large apparent contact angles ($> 150°$) but strong droplet adhesion, allowing water droplets to hang upside down.[96] This phenomenon is vividly demonstrated by the red rose petal surface, which features periodic micropapillae decorated with nanoscale folds (Figs. 6(a) and 6(b)), achieving a superhydrophobic contact angle of 152.4° (Fig. 6(c)) while firmly adhering to water droplets even when inverted (Fig. 6(d)). Mechanistically, this state arises from partial liquid penetration into the random micro-voids (a transitional Cassie-impregnating state). The stochastic distribution of pinning sites creates a discrete but dense pinning network, which generates massive CAH.[96] Experimental analysis confirms that increasing substrate roughness significantly increases the advancing contact angle while the receding angle remains stable, resulting in a sharp surge in hysteresis. The adhesion strength is strictly dictated by the density of these random pinning points.[97] This phenomenon highlights the limitation of stochastic roughness: while it can achieve static superhydrophobicity, it lacks the directional control required for dynamic fluid transport, necessitating the shift toward ordered architectures.

3.2. Ordered open architectures: anisotropic wetting

To overcome the chaotic pinning dynamics of stochastic surfaces, ordered open architectures — specifically parallel grooves and chemically striped patterns — have been developed. Unlike random roughness, these structures impose a deterministic and orthogonal energy landscape on the contact line. This symmetry breaking enables anisotropic wetting, where the droplet exhibits distinct contact angles $(\theta_{\parallel} \neq \theta_{\perp})$ and mobility depending on the direction relative to the texture.

Ordered topographic features, specifically microgrooves, induce anisotropy by imposing direction-dependent energy barriers on contact line motion. When a droplet travels perpendicular to the grooves, the three-phase contact line is forced to undergo a continuous, high-energy "pinning–depinning" cycle as it crosses each ridge. This process significantly increases contact line tortuosity and energy dissipation, acting as a "hydraulic brake" that reduces droplet flow velocity by approximately 50% due to intense pinning forces.[98] In stark contrast, motion parallel to the grooves follows continuous energy troughs. In the Cassie state, the trapped air cushions effectively replace the solid–liquid interface with a shear-free liquid–air interface. This "slip boundary layer" minimizes hydrodynamic drag, enhancing flow velocity by about 15%.[99] This geometric rectification mechanism enables passive, unidirectional liquid transport without external energy input, a principle fundamental to applications in microfluidic drag reduction and directional water harvesting.

Beyond physical topography, chemical heterogeneity using self-assembled monolayers (SAMs) offers a precise method to manipulate contact line pinning at the molecular scale. By patterning alternating hydrophilic and hydrophobic stripes, one can create "virtual" energy barriers without altering surface roughness. On such line-patterned substrates, the contact line experiences asymmetric pinning. Suzuki *et al*. demonstrated that water droplets exhibit significantly lower sliding angles along the stripe orientation compared to the perpendicular direction, confirming that chemical heterogeneity alone produces an effective anisotropic hysteresis landscape.[100] Quantitatively, Morita *et al*. showed that on fluoroalkylsilane-patterned lines, the apparent contact angle differs by more than 10° between longitudinal and transverse directions.[101] This anisotropy arises because the contact line is "clamped" by the hydrophobic domains in the perpendicular direction, whereas it can slide freely along the hydrophilic channels in the parallel direction.

Crucially, the emergence of anisotropic wetting is not an intrinsic property of the pattern itself but is strictly governed by the scale of the heterogeneity relative to the droplet dimensions. Recent theoretical advancements have established a critical scaling law based on the ratio of the stripe width (w) to the contact line length (L). In the regime of fine patterning $(w \ll L)$, the contact line spans a statistically significant number of defects, allowing the system to follow the Cassie–Baxter area-averaging rule and exhibit quasi-isotropic behavior. However, a distinct transition to a pinning-dominated regime occurs as this ratio approaches a critical threshold (typically $w/L > 0.1$). Research indicates that while the classical Cassie equation maintains high predictive accuracy (error $< 5\%$) below this limit, the approximation breaks down significantly above it as the local interaction begins to dominate.[102,103] In this coarse-patterning regime, the contact line becomes discretely pinned by individual stripes, necessitating a shift from global energy averaging to a localized analysis of discrete pinning events.

3.3. Re-entrant geometries: metastable wetting and oleophobicity

While ordered open architectures effectively manipulate water droplets, they face a fundamental thermodynamic limit when dealing with low-surface-tension liquids (e.g., oils, organic solvents). On intrinsically oleophilic materials (where the Young's contact angle $\theta_{\mathrm{Y}} < 90°$), the capillary force on standard vertical micropillars acts downwards, inevitably pulling the liquid into the texture and causing a spontaneous transition to the fully wetted Wenzel state. To overcome this challenge, re-entrant geometries — topologies featuring overhanging structures such as T-shapes, mushrooms, or inverse trapezoids — have been engineered to enable superoleophobicity and omniphobicity.

The physical principle underlying re-entrant structures is the manipulation of the local geometric angle to satisfy the Gibbs pinning criterion. According to the pioneering theory established by Tuteja *et al*.,[104,105] for a liquid to be suspended in the Cassie state, the local contact angle θ_{local} at the texture edge must fulfill the condition

$$\theta_{\mathrm{local}} < \theta_{\mathrm{A}} + \psi - 90°, \tag{11}$$

where ψ is the geometric angle of the texture edge (texture angle). Standard pillars possess a geometric angle of $\psi = 90°$, which cannot effectively support liquids with $\theta_{\mathrm{Y}} < 90°$. However, re-entrant structures feature overhanging edges where ψ effectively exceeds 90°. This topology causes the liquid meniscus to bend upward at the TCL, generating a vertical upward component of capillary force.[106] This force counteracts the Laplace pressure and gravity, effectively "pinning" the oil droplet at the edge of the overhang. Consequently, even if the material itself is intrinsically oleophilic, the macroscopic surface can exhibit contact angles exceeding 150°.[107]

The evolution of re-entrant designs demonstrates the pursuit of extreme pinning robustness against wetting transitions. (i) Simple re-entrant (T-shaped/mushroom): These structures provide a single pinning edge. Although effective for liquids

with moderate surface tension, they may lose their pinning capability under high external pressure if the meniscus sags and touches the pillar shaft. Hensel *et al*. experimentally verified that mushroom-shaped pillars exhibit a breakthrough pressure approximately 30% higher than T-shaped pillars of equivalent dimensions.[108] This enhanced stability is attributed to the continuous curvature of the mushroom cap, which eliminates stress concentrations at sharp corners and ensures more uniform meniscus pinning. (ii) Doubly re-entrant structures: To prevent irreversible wetting, Liu and Kim developed doubly re-entrant structures (e.g., "serpentine" edges) that provide multiple pinning lines.[109] Even if the meniscus depins from the top edge, it is captured by the secondary overhang below. This topology has been shown to sustain the Cassie state for fluorinated liquids with surface tensions as low as 10 mN/m, achieving super-repellency on completely wetting materials.[109]

The practical utility of re-entrant structures is defined by their breakthrough pressure (P_{break}), the critical pressure required to force liquid into the cavities. Theoretical models derived from the force balance at the re-entrant edge indicate that P_{break} is inversely proportional to the spacing and directly related to the overhang length.[110] However, this metastable state remains fragile; localized defects or external impacts can trigger a "sagging" transition. Recent studies have highlighted the "springboard effect" in flexible re-entrant structures, where elastic deformation absorbs kinetic energy during droplet impact, suggesting that structural stiffness is as critical as topological shape in maintaining omniphobicity.[106] In summary, re-entrant engineering demonstrates that in the regime of low-surface-tension wetting, it provides a universal strategy for designing omniphobic surfaces independent of substrate properties.

3.4. Topological regulation: the limits of classical wetting

The discovery of topological wetting states has fundamentally extended the boundaries of traditional wetting theory.[28,65] In this context, the term "topological" explicitly designates the global connectivity of a closed-loop defect (i.e., topological genus $g = 1$), which acts as a continuous macroscopic constraint rather than merely isolated geometric edge-pinning. While classical models predominantly focus on surface chemistry and random roughness, recent breakthroughs demonstrate that the introduction of closed-loop topological defects — such as nanowalls or nanochannels — enables the precise manipulation of contact angles on intrinsically superhydrophilic surfaces. Unlike localized energy barriers generated by stochastic roughness, chemical heterogeneity, or the overhang-dependent mechanics of re-entrant structures, this unique topology anchors the contact line simultaneously across its entire perimeter. This topological control facilitates a deterministic transition from a fully spread regime to highly hydrophobic states ($> 130^\circ$), challenging the fundamental assumptions of continuum wetting mechanics.[28,65]

The physical origin of this anomalous phenomenon lies in the strong pinning effect induced by topological invariance on the TCL.[65] Unlike open grooves or open textures where the contact line can continuously depin, a closed-loop topology imposes a global constraint. Figure 7 illustrates this mechanism vividly. On UV/ozone-treated hydrophilic surfaces, water droplets do not spread indefinitely but are arrested in a metastable configuration known as the "ring-*n* Wenzel state" (Fig. 7(i)). Molecular dynamics simulations (Figs. 7(j3)–7(m3)) reveal that the sharp geometry at the loop's edge creates a severe discontinuity in the molecular force field. This generates a massive energy barrier that "anchors" the droplet edges, resulting in the concentric ring profiles shown in Figs. 7(a)–7(h).

Crucially, experimental verification (Fig. 7) demonstrates that this critical contact angle (θ_{crit}) is remarkably independent of local curvature. The data curves for diverse geometries — circles, triangles, squares, pentagons, and even irregular shapes — overlap significantly. This implies that the topological genus (hole count), rather than specific geometric details, is the dominant order parameter governing the wetting state. To rigorously substantiate that this phenomenon is genuinely governed by topological connectivity rather than mere localized edge-pinning, comparative control cases are critical. When the continuity of the loop is disrupted — such as in open rings, broken loops, or structures with intentional gap defects — the global constraint is fundamentally broken (i.e., transitioning from genus $g = 1$ to $g = 0$). In these defective structures, even if the local edge angles remain geometrically identical, local meniscus depinning occurs readily at the gaps. The liquid sequentially breaches these discontinuities, completely unable to sustain the highly hydrophobic metastable state observed in their closed-loop counterparts. This stark contrast definitively isolates structural connectivity as the prerequisite for this anomalous wetting behavior.

One of the most significant implications of topological wetting is that it reveals the limitations of the classical Young–Gibbs equation at the microscopic scale.[65] According to classical theory, on a hydrophilic surface with a geometric edge angle of $\phi = 90^\circ$, the critical contact angle should not exceed 90°. However, experimental observations reveal a dramatic deviation: when micron/nanoscale droplets are confined to a closed loop with right-angled edges, θ_{crit} can reach as high as 131.3°. This represents a deviation of more than 40% from the theoretical prediction.

Mechanistic studies attribute this discrepancy to the synergistic effect of atomic-scale interactions and specific edge configurations. For instance, simulations show that the edge configuration of a face-centered cubic (FCC) crystal plane can

raise θ_{crit} to 141.3°, whereas a simple cubic structure only reaches 102.9°. To reconcile this cross-scale discrepancy, a modified topological wetting equation has been proposed:[65]

$$\cos\theta_{crit} = \sin(\phi - 90^\circ) - \Omega, \tag{12}$$

where ϕ denotes the geometric edge angle of the topological loop (e.g., 90° for right-angled edges), and Ω represents the additional contact angle offset induced by topological edge effects. Research indicates that for structures maintaining the same topological genus ($g = 1$), Ω is positively correlated with geometric dimensions such as the loop height (h) and the critical channel width w_{crit}, effectively quantifying the cross-scale mutation of wetting behavior caused by topological constraints.

Beyond fundamental theory, the rigid control offered by topology provides a robust platform for functional applications. The contact angle within a closed loop exhibits dynamic programmability, capable of discrete jumps between "*n*-loop" states during growth or continuous, reversible modulation from ~ 130° to 55° during evaporation.[65] Recent breakthroughs have extended this programmability from *in situ* retention to rapid directional transport. By engineering asymmetric topological barriers — often termed "topological liquid diodes" — researchers have successfully broken the symmetry of the contact line to rectify capillary forces. This mechanism enables spontaneous, high-speed fluid transport and "pancake bouncing" phenomena without external energy input, fundamentally overcoming the trade-off between pinning adhesion and sliding mobility.[111,112]

This capability has catalyzed innovations in microfluidics and biomedical engineering. For example, microdroplets can maintain a hydrophobic state $\theta > 90^\circ$ within the loop to inhibit reactant diffusion, optimizing microreactor efficiency. In biomedical bonding, strategies mimicking topological pinning — such as Wang's planar chemical heterogeneity[28] and Yang's "molecular suture" networks[113] — have achieved exceptional tissue adhesion without physical puncture. Furthermore, the ability to guide droplet arrays using special-shaped topologies (Figs. 7(a)–7(h)) offers a novel pathway for the directional deposition of functional materials, showing immense potential in the fabrication of next-generation printed electronics and optical microlens arrays.[65]

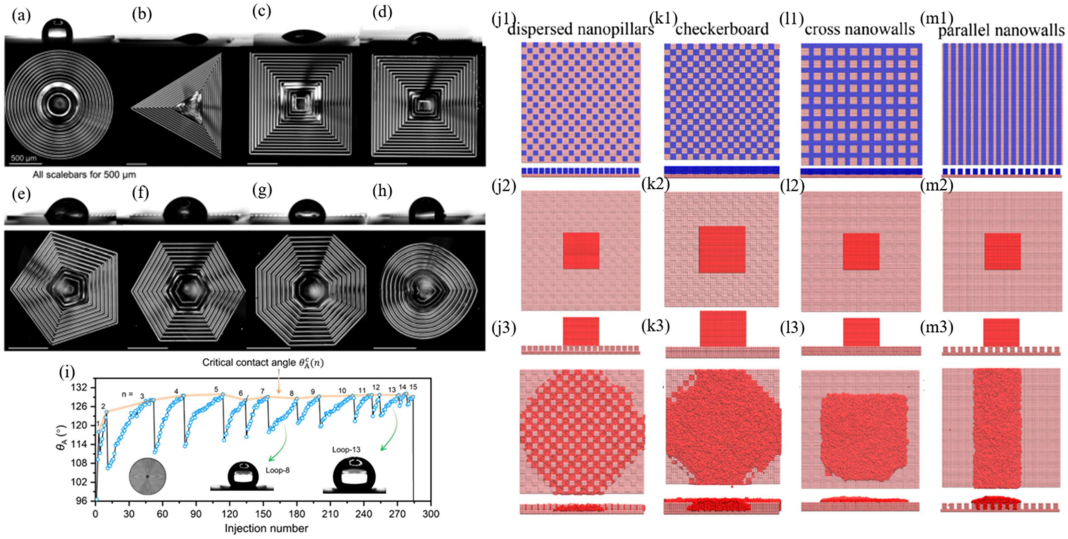

Fig. 7. Annular contact profiles of water droplets on UV/ozone-treated hydrophilic rough surfaces with closed-loop microwalls/microchannels of different geometries. (a)–(h) Droplet shapes and critical contact angles on circle, triangle, square, rectangle, pentagon, hexagon, octagon, and heart-shaped microstructures. (i) Microscopic top view of a ring-shaped contact profile, where the white rings show the microchannel holding the TCL. Scale bars: 500 μm. (j1)–(m1) Bare surface structures; (j2)–(m2) initial placement of a water cube (~ 25600 molecules) on the surface; (j3)–(m3) final states after >12 ns molecular dynamics simulations (water in red, surface atoms in blue/pink). (i, right) Variation of critical contact angle θ_c (n) with droplet injection number, with $\theta_c(n)$ marking transitions between successive loop-Wenzel states.[65,114] (Panels (a)–(i) reproduced with permission from Ref. [65] Copyright 2024, Proceedings of the National Academy of Sciences USA. Panels (j1)–(m3) reproduced with permission from Ref. [114] Copyright 2020, American Chemical Society).

4. Advanced characterization and multiscale modeling

The elucidation of the complex wetting mechanisms discussed in the preceding sections — from the thermodynamic metastability of re-entrant geometries to the limitations of classical theory in describing topological-defect-induced wetting — calls for advanced methodologies in characterization and modeling. Characterizing these non-equilibrium states benefits from moving beyond simple static observation to a comprehensive framework combining high-resolution dynamic metrology, nanoscale imaging, and multiscale numerical simulation, as systematically illustrated by the multiscale platform in Fig. 8. To provide a clearer methodological framework, the advanced characterization and modeling techniques discussed in this section are summarized and compared in Table 1 according to their operational scale, primary information obtained, and representative applications in wetting research.

Table 1. Methodological framework comparing advanced characterization and multiscale modeling approaches for wetting phenomena.

Operational scale	Technique	Primary information obtained	Key capabilities	Target applications
Atomic/Sub-nano	Molecular dynamics (MD)	Atomic interaction, TCL force	Resolving atomic-scale interactions and contact-line force distributions.	Isolating the contribution of atomic edge configurations and substrate lattices to pinning forces.
Nanoscale	Cryo-EM	Liquid–solid interface morphology	Direct visualization of liquid–solid interface configurations.	Revealing nanoscale pinning mechanisms without optical diffraction limits.
	Femtosecond interferometry	Ultrafast contact-line motion	Capturing ultrafast, quantized transitions in contact line motion.	Providing physical basis for dynamic hysteresis and nanocurvature effects.
Micro/Mesoscale	Phase-field modeling (CHNS)	Interface evolution	Capturing transient wetting dynamics, interface evolution, and contact-line motion.	Tracking dynamic droplet coalescence and anisotropic wetting without explicit boundary meshing.
Macroscopic/Continuum	Surface Evolver	Equilibrium interface configuration	Equilibrium interface morphology through interfacial free-energy minimization.	Reproducing static Cassie–Baxter/Wenzel configurations and metastable morphologies.
	ADSA-P	Dynamic contact angle, CAH	High-precision numerical integration of the Laplace equation ($\pm 0.1^\circ$ accuracy).	Resolving low-speed dynamic energy barriers and stick–slip motion of contact lines.
	Stood-up drop (SUD)	Receding angle, depinning threshold	Needle-free receding angle quantification.	Eliminating needle-induced Marangoni artifacts; resolving contact line depinning.
Multiscale	Machine learning (AI/PINN)	Structure–property relationship	Data-driven prediction, surrogate modeling, and inverse design.	Optimizing topological microstructures for specific functionalities (e.g., anti-icing).

The primary obstacle in experimental validation lies in the limitations of traditional goniometry. Standard tangent-fitting methods are subject to inherent human errors and optical diffraction limits, effectively "low-pass filtering" the subtle dynamic features of wetting. For instance, on polypropylene–maleic imide copolymer surfaces, static data dispersion reaches $\pm 6^\circ$, a discretization that high-speed imaging reveals to be caused by the stick–slip motion of the contact line and polymer-induced droplet deformation.[115] Furthermore, time-varying interactions, such as formamide-induced swelling, cause the contact angle to drift at a rate of $0.5^\circ \cdot s^{-1}$, rendering single static measurements thermodynamically unreliable. To resolve these features, axisymmetric droplet shape analysis (ADSA-P) has been established as the gold standard. Unlike geometric fitting, ADSA-P numerically integrates the Laplace equation of capillarity to fit the entire droplet profile, utilizing over 1000 coordinate points to achieve a measurement accuracy of $\pm 0.1^\circ$.[116] However, recent investigations by Dekker and Lohse highlight that even with such algorithms, uncontrolled evaporation in standard pendant/sessile drop measurements can induce significant surface tension gradients (Marangoni flows), necessitating strict environmental control to prevent data artifacts. To eliminate these needle-induced artifacts and symmetry breaking, Vollmer *et al*. recently introduced the "stood-up drop" (SUD) technique. By utilizing a short liquid jet to generate a pancake-shaped spreading film, this method allows for the needle-free quantification of receding contact angles with high reproducibility, specifically resolving the contact line depinning dynamics on defects.[117] This robust, needle-free measurement workflow is directly visualized in Fig. 8(b). This precision allows for the unique capability of capturing the dynamics inherent to topological pinning. By synchronizing with real-time monitoring, ADSA-P can detect instantaneous contact angle fluctuations (spikes $> 8^\circ$) associated with solvent-induced polymer recrystallization (e.g., in diiodomethane–polycaprolactone systems), providing the granular data necessary to verify dynamic energy barriers.[116,118] Validation experiments on FC-722 surfaces further confirm that such low-speed dynamic measurements $\left(0.14\ \mathrm{mm \cdot min^{-1}}\right)$ yield thermodynamic contact angles (118.4°) in excellent agreement with static values, demonstrating their efficacy in substituting error-prone static methods.[119]

While ADSA-P refines macroscopic measurements, validating the concepts of line tension and nanocurvature requires resolving the TCL at the nanometer scale. Measurement errors at this scale primarily stem from topological and chemical deviations. First, nanoscale roughness induces severe pinning; even atomically smooth surfaces like single-layer graphene average roughness ($Ra < 0.5$ nm) exhibit molecular-level inhibition, contributing to significant error formation.[120] Second, chemical heterogeneity can generate hysteresis energy exceeding 100 $\mathrm{mJ \cdot m^{-2}}$ although this can be mitigated to $< 10\ \mathrm{mJ \cdot m^{-2}}$ by lubricating defects with perfluoropolyether.[90,121] To visualize these pinning mechanisms directly, *in situ* cryo-electron microscopy (cryo-EM) provides a promising approach for observing the liquid–solid interface configuration without the ambiguity of optical resolution. Furthermore, regarding the ultrafast dynamics of the contact line, recent studies utilizing femtosecond laser

interferometry have revealed a quantized transition in motion on hydrophobic surfaces. This provides a new quantum-mechanical explanation for dynamic hysteresis that challenges continuous scale models,[122,123] offering a physical basis for the "nanocurvature effect" where the radius of curvature at 10 nm can reduce the contact angle by a maximum of 10%.

Given the experimental difficulties in isolating single-factor influences at the atomic scale, numerical simulations serve as an indispensable "virtual microscope" to deconstruct the mechanisms identified in Section 3. Molecular dynamics (MD) simulations provide the exclusive means to probe the principle at the angstrom level. As highlighted in Subsection 3.4, experimental observations of topological wetting often convolve surface roughness with chemical heterogeneity. MD enables direct visualization of the three-phase contact line at atomic resolution, as demonstrated in Fig. 8(a), allowing for the construction of idealized systems to isolate the contribution of atomic edge configuration and substrate lattice symmetry to the pinning force.[124]

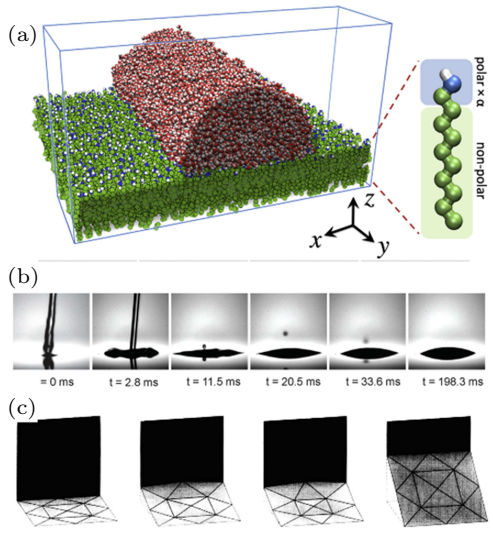

Fig. 8. Multiscale characterization and modeling framework for wetting phenomena. (a) All-atom molecular dynamics simulation of a water nanodroplet on a functionalized surface, revealing the atomic-scale structure of the three-phase contact line. (b) High-speed imaging sequence of the needle-free stood-up drop (SUD) technique for measuring receding contact angles, eliminating needle-induced artifacts. (c) Evolution of capillary surface and contact angle in the Surface Evolver simulation, from initial planar state to energy-minimized equilibrium configuration.[76,117,126] (Reproduced with permission from Ref. [76] Copyright 2017, AIP Publishing. Adapted with permission from Ref. [126] Copyright 1992, Jones and Bartlett Publishers, Inc. Panel (b) reproduced from Ref. [117] under a Creative Commons Attribution 3.0 Unported Licence. Copyright 2026, Royal Society of Chemistry).

At the continuum level, the Surface Evolver method remains one of the most effective approaches for evaluating static morphologies. By minimizing the total interfacial free energy under geometric constraints, it accurately reproduces Cassie–Baxter and Wenzel configurations and has been successfully applied to the design of micro-structured membranes and hierarchical interfaces.[125,126] The energy-minimization principle and equilibrium wetting morphology obtained from Surface Evolver are exemplified in Fig. 8(c).

Concurrently, phase-field models based on the Cahn–Hilliard/Navier–Stokes (CHNS) formulation provide a continuous representation of fluid–fluid interfaces. By introducing a diffuse interface order parameter, this framework captures transient interface evolution, droplet coalescence, and anisotropic wetting behaviors under electric or chemical gradients without the need for explicit contact line tracking.[127,128] Integrating these multiscale methodologies provides the comprehensive framework needed to predict the complex behaviors of topological wetting surfaces. Furthermore, the emergence of artificial intelligence (AI) and physics-informed neural networks (PINN) has revolutionized this landscape. Unlike traditional simulations that rely on forward solving of governing equations, deep learning approaches can correlate surface morphology and chemistry with wettability to achieve inverse design of topological patterns.[129] By training on high-fidelity datasets generated from MD or experiments, these data-driven models can rapidly predict contact angle hysteresis and optimize microstructures for specific functionalities, such as anti-icing or fog harvesting, accelerating the materials discovery cycle by orders of magnitude.

5. Applications: functionalization via contact angle engineering

The transition from fundamental wetting theories to practical applications relies on the precise engineering of the TCL. By manipulating topological pinning and energy barriers — as elucidated in Section 3 — contact angle control has evolved from passive surface modification to active functionalization. Crucially, modern applications no longer rely merely on global wettability, but specifically exploit the manipulation of contact line pinning, wetting energy barriers, and topological confinement. This paradigm shift is revolutionizing fields ranging from anti-icing systems to microfluidic reactors.

5.1. Anti-icing and de-icing: thermodynamic delay and low adhesion

The accumulation of ice entails a complex interplay between condensate nucleation and interfacial adhesion. The physical basis for anti-icing lies in optimizing wettability parameters (contact angle (CA) $> 150°$, rolling angle (RA) $< 10°$, CAH $< 5°$) to inherently inhibit the Wenzel transition of supercooled droplets and minimize the fracture energy of the ice–solid interface.

Thermodynamic nucleation suppression Micro/nano composite structures constructed by femtosecond lasers, such as "burr-like" architectures, maintain a robust Cassie–Baxter state by reducing the solid–liquid area fraction to approximately 4%.[130] Specifically, the micron-scale burrs (Figs. 9(g)

and 9(h)), with a local radius of curvature $R_c < 1$ μm, impose a severe thermodynamic barrier that suppresses heterogeneous nucleation. Consequently, the Siberian-Cocklebur composite structure extends the freezing time at −10 °C to 334 s, compared to only 120 s for bare glass.[131,132]

Minimizing adhesion strength When freezing is inevitable, the strategy shifts to reducing ice adhesion strength (τ_{ice}) through stress concentration. As demonstrated by the square column arrays in Fig. 9(d), discrete topographical features induce stress singularities at the crack tip during de-icing. This structural design effectively reduces τ_{ice} from 800–1200 kPa on bare aluminum to 10–30 kPa on superhydrophobic surfaces.[133] Notably, aluminum-based composite nanopore structures can further reduce this to an ultra-low 0.71 kPa.[134] However, as critically reviewed by Kreder *et al.*, classical superhydrophobicity may become less effective under high humidity due to frost formation, necessitating strategies that fundamentally distinguish between mechanisms for repelling liquid water and those for delaying ice nucleation.[135]

Active de-icing synergy To address the severe contact line pinning of frozen droplets under extreme conditions, active strategies are integrated to dynamically alter the interfacial energy landscape. Photothermal TiN coatings can reach 70 °C under 1 solar intensity, reducing de-icing energy consumption by 73.6% by melting the pinned ice-solid contact line.[136] Similarly, graphene-based electrothermal films achieve rapid de-icing (3 min at 12 V), creating a "slippery" interfacial water layer that drastically lowers the depinning energy barrier, maintaining low adhesion.[137] Future challenges focus on maintaining the stability of the submicron air film (plastron) under environmental pressure and developing adaptive magnetically responsive arrays for on-demand morphological switching.[138,139]

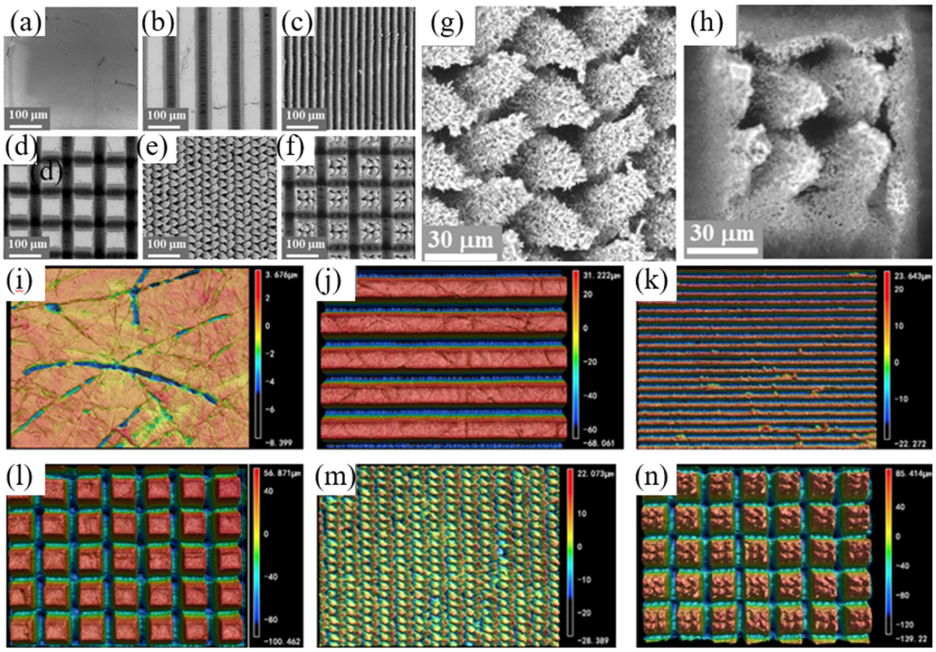

Fig. 9. Morphological evolution and three-dimensional property characterization of super-ice micro/nano structures. (a)–(f) SEM morphology of microstructures on different laser-processed surfaces: (a) primitive polytetrafluoroethylene (PTFE); (b) parallel fringes; (c) high-density linear arrays; (d) square column array; (e) honeycomb structure; (f) nano lattice. (g)–(h) Close-up of burr-like composite structure: (g) ball crown body (25 μm diameter) with surface burr; (h) micron-scale burr topography (induces Cassie state stabilization). (i)–(n) The three-dimensional surface property analysis (confocal microscopy): (i)–(k) roughness distribution of fringe, square column, honeycomb structures (color scale: height 0–35 μm); (l)–(n) composite structure curvature and contact area fraction plot.[140] (Reproduced from Ref. [140] under the CC-BY license. Copyright 2021, Elsevier).

5.2. Microdroplet reactors: active actuation and topological confinement

In the realm of microchemistry, the precise manipulation of the contact angle serves as the "engine" for droplet transport, mixing, and reaction confinement. This is achieved through two parallel mechanisms: active field-induced actuation and passive topological confinement.

Active actuation Electrowetting-on-dielectric (EWOD) modulates the contact angle θ by altering the electric double-layer energy, which effectively lowers the local macroscopic pinning barrier to drive droplet motion. This is theoretically described by the Young–Lippmann equation[141]

$$\cos\theta_V = \cos\theta_Y + \frac{\varepsilon_0\varepsilon_r}{2d\gamma_{LV}}V^2, \tag{13}$$

where θ_Y is the initial contact angle, ε_0 and ε_r are the vacuum and relative permittivities of the dielectric layer, d is the layer thickness, and V is the applied voltage. While this equation predicts a continuous decrease in contact angle with volt-

age, practical applications often encounter contact angle saturation due to effects such as dielectric breakdown or charge trapping.[142–144] Recent advances utilizing modified thermodynamic models have enabled precise actuation, where electrode arrays drive cooling microdroplets to enhance chip heat dissipation efficiency by 210.7%.[145] Beyond electric fields, light-responsive surfaces (e.g., liquid crystals) allow for non-contact control; near-infrared driven microvalves can switch wettability in milliseconds, enabling the on-demand delivery of reagents like dopamine.[146]

Topological confinement Topological defects act as "virtual walls" to confine reactants, enhancing local concentration and kinetics. This precise compartmentalization fundamentally increases assay sensitivity by elevating the effective concentration of rare species, enabling unprecedented high-throughput applications such as single-cell and single-molecule screening at kilohertz speeds.[147] In electrowetting chips, precise droplet merging reduces mixing time to the millisecond level, enhancing the oxidation rate of aniline by a factor of five. In biochemical detection, optimizing capillary forces within microcapillary arrays substantially improves enzyme-linked immunosorbent assay (ELISA) signal intensity by accelerating antigen–antibody binding kinetics.[148–150] Furthermore, the "superhydrophobic confinement effect" ($\theta > 150°$) suppresses the coffee-ring effect, ensuring uniform particle deposition. This mechanism has been applied to synthesize monodisperse gold nanoparticles on silver films[151] and to align carbon nanotubes, increasing composite shear strength from 65 MPa to 135 MPa.[152] Notably, AI-assisted design is emerging as a new paradigm, where machine learning optimizes micropillar arrays to predictively build θ-adhesion mapping models for adaptive microreactors.

5.3. Self-cleaning: anisotropic wetting and photocatalytic synergy

Self-cleaning surfaces exploit the energy balance at the interface to achieve either the passive removal of contaminants (lotus effect) or their active decomposition.

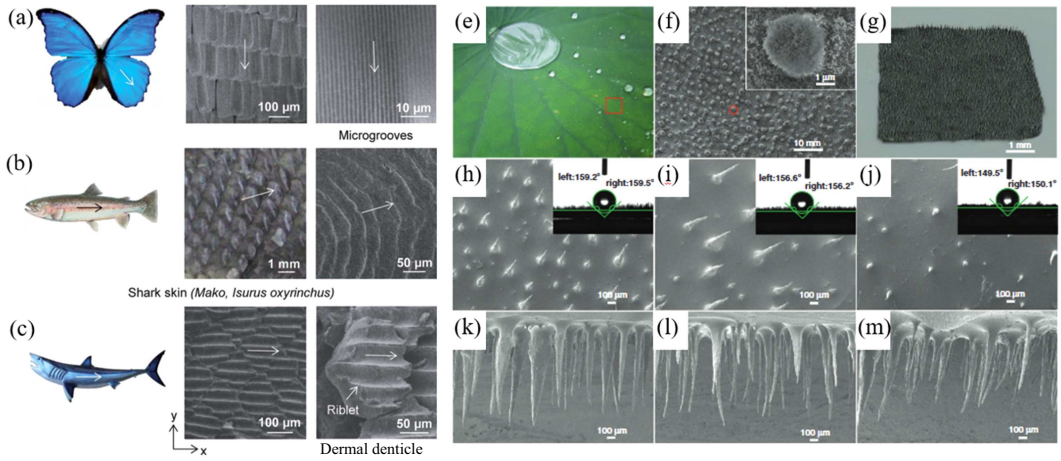

Fig. 10. Superhydrophobic surface and biomimetic design in nature. (a) Parallel microgrooves of the wings of the large flash butterfly (arrow, bar = 100 μm); (b) Mako shark skin grooved dermal tooth (bar = 1 mm); (c) Dermal denticle magnification detail (bar = 50 μm). Lotus leaf and biomimetic structure: (d) lotus leaf prototype; (e) foliar papillary protrusions, SEM (red framed area); (f) enlargement of papillary protrusions (with single-structure illustration); (g) biomimetic ciliary array (Pem-iCM). Effect of aspect ratio on hydrophobicity: (h)–(j) Bionic cilia top-down SEM (aspect ratio 47/25/13, contact angle 159.2° /156.6° /149.5°); (k)–(m) cilia cross-section SEM.[165,166] (Panels (a)–(c) reproduced with permission from Ref. [165] Copyright 2013, Royal Society of Chemistry. Panels (e)–(m) reproduced from Ref. [166] under the Creative Commons Attribution 4.0 International License.)

Biomimetic anisotropy The core requirement for rolling-mode self-cleaning is minimizing hysteresis ($< 5°$). As systematically reviewed by Quéré, introducing specific microtextures onto solid surfaces fundamentally alters the force balance at small scales, transforming ordinary substrates into "non-sticking" super-hydrophobic states governed by unusual droplet dynamics.[153] Bio-inspired hierarchical structures play a pivotal role in this regard. As illustrated in Fig. 10, the parallel microgrooves of butterfly wings (Fig. 10(a)) and rice leaves induce a robust Cassie–Baxter state, reducing the sliding angle (SA) to 3°–6°.[154] Similarly, the grooved dermal teeth of sharks (Figs. 10(b) and 10(c)) are optimized to increase the critical Weber number ($We > 100$), preventing the kinetic impalement of droplets (Wenzel transition) during impact.[155] Crucially, the geometric aspect ratio (AR) dictates the stability of these states; as evidenced by the biomimetic ciliary arrays in Figs. 10(g)–10(m), increasing the AR from 13 to 47 directly enhances the contact angle from 149.5° to 159.2° (Figs. 10(h) and 10(j)), confirming that deeper topological cavities raise the energy barrier. To address the mechanical fragility often associated with such high-aspect-ratio structures, Wang *et al.* (Ras group) established a standardized wear protocol and proposed "armored" microstructures to physically shield the fragile nanotexture,[156] defining a new benchmark for durability. In parallel strategies, honeycomb-like SiO_2/PDMS coatings demonstrate re-

markable durability, maintaining CA $> 150°$ after 500 wear cycles.[157] Furthermore, integrating the liquid-infused concept with inverse colloidal monolayers creates interconnected, honeycomb-like nanoporous structures that not only firmly lock in lubricants for defect-tolerant self-repair, but also maintain high optical transparency, making them highly suitable for self-cleaning solar cells and optical devices.[158] Meanwhile, paraffin-coated structures stabilize CAH at 6° by minimizing surface energy gradients.[159]

Photocatalytic hydrophilicity Complementary to the low-pinning superhydrophobic state, superhydrophilic surfaces (TiO_2-based) utilize light-induced reactions to effectively eliminate the contact line pinning energy barrier entirely. This extreme depinning allows water to spontaneously form a continuous sheeting film to wash away contaminants. Strategies such as Fe^{3+}/Al^{3+} doping and $BiOI/TiO_2$ heterojunctions have expanded the photo-response to the visible spectrum, enhancing efficiency by 40%.[160,161] Intelligent dual-function surfaces, such as flower-like TiO_2/OTMS coatings, combine the benefits of high static contact angles with UV-triggered contaminant degradation.[162] The efficiency of self-cleaning is quantitatively defined by the area ratio of removed contaminants, providing a theoretical benchmark that guides the design of surfaces for industrial applications, from photovoltaic panels (where coatings increase power recovery by 200%[163]) to self-healing smart textiles.[164]

6. Conclusion and outlook

This review highlights the shift in wetting science from classical thermodynamics to topological wetting. We emphasize that the static contact angle is not simply a material constant, but a variable governed by energy barriers at the TCL. As classical equations show deviations on closed-loop microstructures, geometrical confinement can dominate apparent wetting behavior under metastable conditions. Shifting the focus from global interfacial tension to local contact line pinning provides a practical framework for understanding CAH, metastability, and droplet dynamics, addressing several limitations inherent in classical models.

Developing a unified theory for extreme non-equilibrium conditions remains a challenge. Current theoretical frameworks struggle to describe the coupling between interfacial viscoelasticity and line tension in complex fluids, particularly in nanoparticle-laden electrolytes or high-shear environments. A persistent practical issue is the durability–functionality trade-off: the high-aspect-ratio structures required for superrepellency are mechanically fragile. Furthermore, predicting Cassie state transitions requires predictive models capable of capturing environmental stress effects. The relationship between wettability fluctuations and functional performance in systems like proton exchange membranes also warrants quantitative study.

Addressing these limitations requires combining multiscale characterization with data-driven design. Future progress depends on observing dynamic processes at the nanoscale. For instance, coupling *in situ* microscopy with molecular dynamics (MD) simulations can help visualize the contact line pinning that drives macroscopic hysteresis. Resolving these nanoscale stick–slip dynamics is necessary to accurately evaluate contact line energy balances. Concurrently, machine learning approaches can shift from property prediction to inverse design. Training models on high-fidelity experimental data can identify topological patterns that optimize nucleation barriers or capillary forces, thereby reducing reliance on trial-and-error iterations.

The field is also advancing toward adaptive interfaces. Future gradient systems may incorporate self-healing chemistries and distinct topological zones to facilitate autonomous droplet transport. These developments shift wetting science from descriptive studies of interfacial tension toward engineering approaches based on dynamic contact line energy. This perspective supports practical applications across biomedical implants, energy conversion, and smart manufacturing.

Acknowledgements

D. L. would like to acknowledge the National Natural Science Foundation of China (Grant No. 12674264), the Ningbo Youth Science and Technology Innovation Leading Talent Project (Grant No. 2025QL005), the Natural Science Foundation of Zhejiang (Grant No. LMS26A040007), the Natural Science Foundation of Ningbo (Grant No. 2024J198), and the Fundamental Research Funds for the Provincial Universities of Zhejiang.

References

[1] Zhang X, Ben S, Zhao Z, Ning Y, Li Q, Long Z, Yu C, Liu K and Jiang L 2023 *Adv. Funct. Mater.* **33** 2212217
[2] Zhang G, Ma L, Tong B, Liang F, Wang X, Hu E and Dearn K 2023 *Int. J. Hydromechatronics* **6** 380
[3] Liu X, Jia L, Ding Y, Dang C, Yin L, Xu J and Zhang R 2024 *ACS Appl. Mater. Interfaces* 16 56293
[4] Hao S, Zhao Z, Xie Z, Li Z, Liu J, Wu F and Kou J 2025 *Appl. Phys. Lett.* **126** 021601
[5] de Gennes P G 1985 *Rev. Mod. Phys.* **57** 827
[6] Young T 1805 *Philos. Trans. R. Soc. Lond.* **95** 65
[7] Ma C, Chen C, Xu Z, Lv C and Zheng Q 2021 *Extreme Mech. Lett.* **48** 101388
[8] Johnson M F G, Schluter R A and Bankoff S G 1997 *Rev. Sci. Instrum.* **68** 4097
[9] Sheiko S S, Muzafarov A M, Winkler R G, Getmanova E V, Eckert G and Reineker P 1997 *Langmuir* **13** 4172
[10] Wang L, Huang H and Lu X 2013 *Phys. Rev. E* **87** 013301
[11] Manservisi S and Scardovelli R 2009 *Comput. Fluids* **38** 406
[12] Rosario R, Gust D, Garcia A A, Hayes M, Taraci J L, Clement T, Dailey J W and Picraux S T 2004 *J. Phys. Chem. B* **108** 12640

[13] Jeon D H 2018 *Trans. KSME B* **42** 429
[14] Jeon D H 2016 *Trans. KSME B* **40** 47
[15] Zhang X, Li J, Ao H, Liu D, Shi L, Wang C, Zhu Y and Qian Y 2020 *Energy Storage Mater.* **30** 337
[16] Zu Y Q, Yan Y Y, Li J Q and Han Z W 2010 *J. Bionic Eng.* **7** 191
[17] Gong W, Yan Y, Chen S and Giddings D 2017 *J. Bionic Eng.* **14** 486
[18] Elbourne A, Dupont M F, Collett S, Truong V K, Xu X, Vrancken N, Baulin V, Ivanova E P and Crawford R J 2019 *J. Colloid Interface Sci.* **536** 363
[19] Misyura S Y 2022 *J. Eng. Thermophys.* **31** 414
[20] Liu Q, Yu J and Wang H 2020 *Int. J. Heat Mass Transf.* **148** 118985
[21] He P and Yao C W 2019 *MRS Commun.* **9** 1060
[22] Zhang Y, Matthews S, Tran A T T and Hyland M 2016 *Surf. Coat. Technol.* **307** 807
[23] Kanduc M, Schneck E and Netz R R 2024 *Phys. Chem. Chem. Phys.* **26** 713
[24] Al Mukahal F H H, Duffy B R and Wilson S K 2015 *Phys. Fluids* **27** 052101
[25] Zeng Q, Zhou H, Huang J and Guo Z 2021 *Nanoscale* **13** 11734
[26] Wong T S, Kang S H, Tang S K, Smythe E J, Hatton B D, Grinthal A and Aizenberg J 2011 *Nature* **477** 443
[27] Li C, Li M, Ni Z, Guan Q, Blackman B R and Saiz E 2021 *J. R. Soc. Interface* **18** 20210162
[28] Wang S, Lin D, Francisco J S, Zeng X C and Gao Y 2024 *J. Am. Chem. Soc.* **146** 28748
[29] Erbil H Y 2021 *Colloids Interfaces* **5** 8
[30] Gibbs J W 1878 *Am. J. Sci.* **16** 441
[31] Sefiane K 2011 *Eur. Phys. J. Spec. Top.* **197** 151
[32] Erbil H Y 2014 *Surf. Sci. Rep.* **69** 325
[33] Marmur A, Della Volpe C, Siboni S, Amirfazli A and Drelich J W 2017 *Surf. Innov.* **5** 3
[34] Huang Z 2020 *Philos. Mag. Lett.* **100** 181
[35] Bormashenko E 2013 *Colloid Polym. Sci.* **291** 339
[36] Friberg S E 2015 *J. Dispers. Sci. Technol.* **36** 160
[37] Wenzel R N 1936 *Ind. Eng. Chem.* **28** 988
[38] Wenzel R N 1949 *J. Phys. Chem.* **53** 1466
[39] Whyman G, Bormashenko E and Stein T 2008 *Chem. Phys. Lett.* **450** 355
[40] Extrand C W 2003 *Langmuir* **19** 3793
[41] Gao L and McCarthy T J 2007 *Langmuir* **23** 3762
[42] Swain P S and Lipowsky R 1998 *Langmuir* **14** 6772
[43] Cassie A B D and Baxter S 1944 *Trans. Faraday Soc.* **40** 546
[44] Milne A and Amirfazli A 2012 *Adv. Colloid Interface Sci.* **170** 48
[45] Marmur A 2003 *Langmuir* **19** 8343
[46] Patankar N A 2003 *Langmuir* **19** 1249
[47] Lafuma A and Quéré D 2003 *Nat. Mater.* **2** 457
[48] Bonn D 2001 *Curr. Opin. Colloid Interface Sci.* **6** 22
[49] Giacomello A, Chinappi M, Meloni S and Casciola C M 2012 *Phys. Rev. Lett.* **109** 226102
[50] Patankar N A 2004 *Langmuir* **20** 7097
[51] Papadopoulos P, Mammen L, Deng X, Vollmer D and Butt H J 2013 *Proc. Natl. Acad. Sci. USA* **110** 3254
[52] Bi L, Wang F and Nestler B 2025 *Phys. Rev. Res.* **7** 043093
[53] Whyman G and Bormashenko E 2011 *Langmuir* **27** 8171
[54] Hensel R, Finn A, Helbig R, Killge S, Braun H G and Werner C 2014 *Langmuir* **30** 15162
[55] Lv P, Xue Y, Shi Y, Lin H and Duan H 2014 *Phys. Rev. Lett.* **112** 196101
[56] Lee C and Kim C J 2011 *Phys. Rev. Lett.* **106** 014502
[57] Quéré D 2008 *Annu. Rev. Mater. Res.* **38** 71
[58] Drelich J 1996 *Colloids Surf. A* **116** 43
[59] Joanny J F and de Gennes P G 1984 *J. Chem. Phys.* **81** 552
[60] Reyssat M and Quéré D 2009 *J. Phys. Chem. B* **113** 3906
[61] Bartell F E and Smith J W 1953 *J. Phys. Chem.* **57** 455
[62] Extrand C W and Kumagai Y 1996 *J. Colloid Interface Sci.* **184** 191
[63] Extrand C W 2002 *J. Colloid Interface Sci.* **248** 136
[64] Erbil H Y and Cansoy C E 2009 *Langmuir* **25** 14135
[65] Lin D, Wang S, Xu W, Chen Y, Li P, Fang Y G, Zhao W, Duan X, Yang X, Jiang Z, Fang W H, Zeng X C, Francisco J S and Gao Y 2024 *Proc. Natl. Acad. Sci. USA* **121** e2315730121
[66] Extrand C W 2002 *Langmuir* **18** 7991
[67] Liu Y M, Wu Z Q and Yin D C 2020 *Colloids Surf. A* **588** 124381
[68] Baldygin A, Ahmed A, Baily R, Ismail M F, Khan M, Rodrigues N, Salehi A R, Ramesh M, Bhattacharya S, Willers T, Gowanlock D and Waghmare P R 2023 *npj Microgravity* **9** 49
[69] Tang Z, Xu B, Wang X and Chen Z 2022 *Microgravity Sci. Technol.* **34** 53
[70] Sommers A and Jacobi A 2008 *J. Colloid Interface Sci.* **328** 402
[71] Wang F, Wu Y and Nestler B 2023 *Adv. Mater.* **35** 2210745
[72] Iwamatsu M 2016 *Phys. Rev. E* **94** 042803
[73] Kubochkin N and Gambaryan-Roisman T 2021 *Phys. Rev. Fluids* **6** 093603
[74] Bonn D, Eggers J, Indekeu J, Meunier J and Rolley E 2009 *Rev. Mod. Phys.* **81** 739
[75] Starov V 2013 *Colloid Polym. Sci.* **291** 261
[76] Kanduc M 2017 *J. Chem. Phys.* **147** 174701
[77] Rusanov A, Shchekin A and Tatyanenko D 2004 *Colloids Surf. A* **250** 263
[78] Saini D and Rao D N 2009 *SPE Reserv. Eval. Eng.* **12** 702
[79] Amirfazli A and Neumann A 2004 *Adv. Colloid Interface Sci.* **110** 121
[80] Marmur A 2022 *Colloids Interfaces* **6** 39
[81] Elhaj M A, Enamul Hossain M, Imtiaz S A and Naterer G F 2020 *J. Pet. Explor. Prod. Technol.* **10** 1897
[82] Nosonovsky M 2007 *Langmuir* **23** 9919
[83] Shardt N and Elliott J A W 2018 *Langmuir* **34** 12191
[84] Adamson A W and Gast A P 1997 *Physical Chemistry of Surfaces*, 6th edn. (New York: John Wiley & Sons) pp. 1–15
[85] Larsen S T and Taboryski R 2009 *Langmuir* **25** 1282
[86] Iglauer S, Salamah A, Sarmadivaleh M, Liu K and Chi P 2014 *Int. J. Greenhouse Gas Control* **22** 325
[87] Belman N, Jin K, Golan Y, Israelachvili J N and Pesika N S 2012 *Langmuir* **28** 14609
[88] Drelich J W 2019 *Adv. Colloid Interface Sci.* **267** 1
[89] Kolodin A N and Bulavchenko A I 2019 *Appl. Surf. Sci.* **463** 820
[90] Jiang H, Mueller-Plathe F and Panagiotopoulos A Z 2017 *J. Chem. Phys.* **147** 084708
[91] Bargir S, Dunn S, Jefferson B, Macadam J and Parsons S 2009 *Appl. Surf. Sci.* **255** 4873
[92] Eliaz N, Shmueli S, Shur I, Benayahu D, Aronov D and Rosenman G 2009 *Acta Biomater.* **5** 3178
[93] Bharathidasan T, Narayanan T N, Sathyanaryanan S and Sreejakumari S S 2015 *Carbon* **84** 207
[94] Gao N and Yan Y 2009 *J. Bionic Eng.* **6** 335
[95] Feng L, Zhang Y, Xi J, Zhu Y, Wang N, Xia F and Jiang L 2008 *Langmuir* **24** 4114
[96] Bormashenko E 2010 *Philos. Trans. R. Soc. A* **368** 4695
[97] Mandsberg N K and Taboryski R 2017 *Surf. Topogr.: Metrol. Prop.* **5** 024001
[98] Sikalo S, Wilhelm H D, Roisman I V, Jakirlic S and Tropea C 2005 *Phys. Fluids* **17** 062103
[99] Kamp M, de Nijs B, Baumberg J J and Scherman O A 2021 *J. Colloid Interface Sci.* **581** 417
[100] Suzuki S, Nakajima A, Tanaka K, Sakai M, Hashimoto A, Yoshida N, Kameshima Y and Okada K 2008 *Appl. Surf. Sci.* **254** 1797
[101] Morita M, Koga T, Otsuka H and Takahara A 2005 *Langmuir* **21** 911
[102] Zhang K, Chen S and Wang Y 2018 *Colloids Surf. A* **539** 237
[103] Zhang K, Zhao J, Chen S, Wang Y and Liu Y 2019 *Appl. Surf. Sci.* **486** 337
[104] Tuteja A, Choi W, Ma M, Mabry J M, Mazzella S A, Rutledge G C, McKinley G H and Cohen R E 2007 *Science* **318** 1618
[105] Tuteja A, Choi W, Mabry J M, McKinley G H and Cohen R E 2008 *Proc. Natl. Acad. Sci. USA* **105** 18200
[106] Deng X, Mammen L, Butt H J and Vollmer D 2012 *Science* **335** 67
[107] Kota A K, Kwon G and Tuteja A 2014 *NPG Asia Mater.* **6** e109
[108] Hensel R, Helbig R, Aland S, Braun H G, Voigt A, Neinhuis C and Werner C 2013 *Langmuir* **29** 1100
[109] Liu T L and Kim C J 2014 *Science* **346** 1096
[110] Chhatre S S, Choi W, Tuteja A, Park K C, Mabry J M, McKinley G H and Cohen R E 2010 *Langmuir* **26** 4027
[111] Zhang B, Li J, Zhou J, *et al.* 2024 *Nature* **628** 84
[112] Zhang Y, Li L, Li G, Lin Z, Wang R, Chen D, Lei Y, Tan D, Wang Z, Zhao Y and Xue L 2025 *Sci. Adv.* **11** eadt9526
[113] Yang J, Bai R and Suo Z 2018 *Adv. Mater.* **30** 1800671

[114] Gao Y, Zhu C, Zuhlke C, Alexander D, Francisco J S and Zeng X C 2020 *J. Am. Chem. Soc.* **142** 18491
[115] Karim A M and Kavehpour H P 2018 *Colloids Surf. A* **548** 54
[116] Zhang D, Wang Y and Gan Y 2013 *Appl. Surf. Sci.* **274** 405
[117] Diaz D, Bhargava A, Walz F, Sharifi A, Summaly S, Berger R, Kappl M, Butt H J, Lohse D, Willers T, Sanjay V and Vollmer D 2026 *Soft Matter* **22** 657
[118] Chen H, Muros-Cobos J L and Amirfazli A 2018 *Rev. Sci. Instrum.* **89** 035117
[119] Schmitt M, Hempelmann R, Ingebrandt S, Munief W M, Gross K, Grub J and Heib F 2015 *J. Adhes. Sci. Technol.* **29** 1796
[120] Kozbial A, Li Z, Conaway C, McGinley R, Dhingra S, Vahdat V, Zhou F, D'Urso B, Liu H and Li L 2014 *Langmuir* **30** 8598
[121] Bormashenko E, Bormashenko Y, Whyman G, Pogreb R, Musin A, Jager R and Barkay Z 2008 *Langmuir* **24** 4020
[122] Geens J, Van der Bruggen B and Vandecasteele C 2004 *Chem. Eng. Sci.* **59** 1161
[123] Emelyanenko A M, Ermolenko N V and Boinovich L B 2004 *Colloids Surf. A* **239** 25
[124] Chen J Z Y 2025 *Soft Matter* **21** 6937
[125] White J, Santos M, Rodríguez-Valverde M and Velasco S 2015 *Langmuir* **31** 5326
[126] Brakke K A 1992 *Exp. Math.* **1** 141
[127] Badillo A 2015 *Phys. Rev. E* **91** 033005
[128] Xu C, Lu Z and Li L 2022 *Front. Energy Res.* **9** 827116
[129] Sharma P, Chung W T, Akoush B and Ihme M 2023 *Energies* **16** 2343
[130] Nguyen B D, Cao B X, Do T C, Trinh H B and Nguyen T B 2021 *J. Adhes.* **97** 860
[131] Fan L, Xia M, Liu J, Li B, Zhu T, Zhao Y, Song L and Yuan Y 2023 *Coatings* **13** 1792
[132] Yuan G, Zhou R, Yan T, Yan H and Liao Q 2024 *J. Manuf. Process.* **110** 41
[133] Zhao Z, Chen H, Zhu Y, Liu X, Wang Z and Chen J 2022 *Compos. Sci. Technol.* **227** 109578
[134] Li B, Bai J, Yang L, Zhang L, Dai X, Zhang C, Hua X, Zhu T, Xiang H, Liao R and Yuan Y 2023 *Coatings* **13** 1859
[135] Kreder M J, Alvarenga J, Kim P and Aizenberg J 2016 *Nat. Rev. Mater.* **1** 15003
[136] Lei Y, Lan H, Jiang B, Yuan Y, Vorontsov D A, Gao G, Zhang Y and Chen Q 2025 *Appl. Surf. Sci.* **680** 161305
[137] Chu Z, Jiao W, Huang Y, Yan M, Zheng Y, Wang R and He X 2020 *Adv. Mater. Interfaces* **7** 2000492
[138] Zhang H, Zhang X, He F, Lv C and Hao P 2022 *Int. J. Heat Mass Transf.* **195** 123196
[139] Shen W, Zhang Z, Xu K, Zhu H, Yang S, Wang J and Liu Y 2025 *J. Colloid Interface Sci.* **680** 464
[140] Ge C, Yuan G, Guo C, Ngo C V and Li W 2021 *Mater. Des.* **204** 109689
[141] Lippmann G 1875 *Ann. Chim. Phys.* **5** 494
[142] Mugele F and Baret J C 2005 *J. Phys.: Condens. Matter* **17** R705
[143] Markodimitrakis I E, Sema D G, Chamakos N T, Papadopoulos P and Papathanasiou A G 2021 *Soft Matter* **17** 4335
[144] Oliveira E, Doering C and Fouckhardt H 2024 *Sens. Actuators A* **365** 114835
[145] Ahmad I, Ranjan A, Pathak M and Khan M K 2022 *IEEE Trans. Compon. Packag. Manuf. Technol.* **12** 288
[146] Beyazkilic P, Akcimen S, Elbuken C, Ortac B, Cai S and Bukusoglu E 2022 *Adv. Funct. Mater.* **32** 2205385
[147] Guo M T, Rotem A, Heyman J A and Weitz D A 2012 *Lab Chip* **12** 2146
[148] Tencer M, Nie H Y and Berini P 2011 *Appl. Surf. Sci.* **257** 4038
[149] Molchanov S P, Roldughin V I, Chernova-Kharaeva I A and Yurasik G A 2016 *Colloid J.* **78** 633
[150] Honkawa M, Fujiki D, Terayama N, Sugiyama M, Saiki T, Sumitomo K and Utsumi Y 2024 *J. Photopolym. Sci. Technol.* **37** 351
[151] Safaee A, Sarkar D K and Farzaneh M 2008 *Appl. Surf. Sci.* **254** 2493
[152] An F, Lu C, Guo J, He S, Lu H and Yang Y 2011 *Appl. Surf. Sci.* **258** 1069
[153] Quéré D 2005 *Rep. Prog. Phys.* **68** 2495
[154] Fernandez A, Francone A, Thamdrup L H, Johansson A, Bilenberg B, Nielsen T, Guttmann M, Sotomayor Torres C M and Kehagias N 2017 *J. Micromech. Microeng.* **27** 045020
[155] Ambrosia M S, Ha M Y and Balachandar S 2013 *Appl. Surf. Sci.* **282** 211
[156] Wang D, Sun Q, Hokkanen M J, Zhang C, Lin F Y, Liu Q, Zhu S P, Zhou T, Chang Q, He B, Zhou Q, Chen L, Wang Z, Ras R H A and Deng X 2020 *Nature* **582** 55
[157] Kumar D, Li L and Chen Z 2016 *Prog. Org. Coat.* **101** 385
[158] Vogel N, Belisle R A, Hatton B, Wong T S and Aizenberg J 2013 *Nat. Commun.* **4** 2176
[159] Kang X, Zi W W, Xu Z G and Zhang H L 2007 *Appl. Surf. Sci.* **253** 8830
[160] Han C, Zhao L, Zhang M, Pan L and Liu Z 2020 *J. Nanosci. Nanotechnol.* **20** 4084
[161] Henriquez A, Melin V, Romero R, Murillo-Sierra J C, Cerna M, Yanez V, Salas B, Cornejo-Ponce L, Pecchi G and Contreras D 2025 *Surf. Interfaces* **65** 106481
[162] Mun Y, Cho S, Jeong E and Bae J S 2020 *Text. Color. Finish.* **32** 158
[163] Fan C, Zeng J, Yan X, Shen Y, Chen J and Wang P 2024 *J. Renew. Sustain. Energy* **16** 063503
[164] Roy S, Zhai L, Kim J W, Kim H C and Kim J 2020 *Prog. Org. Coat.* **140** 105500
[165] Bixler G D and Bhushan B 2013 *Nanoscale* **5** 7685
[166] Liu S, Liu X, Zhou G, Qin F, Jing M, Li L, Song W and Sun Z 2020 *Nat. Commun.* **11** 6158